

Feedback shear layer control for bluff body drag reduction

MARK PASTOOR¹†, LARS HENNING¹,
BERND R. NOACK², RUDIBERT KING¹
AND GILEAD TADMOR³

¹Berlin Institute of Technology ER2–1, Department of Process Engineering, Chair of Measurement and Control, Hardenbergstraße 36a, D-10623 Berlin, Germany

²Berlin Institute of Technology MB1, Department of Fluid Dynamics and Technical Acoustics, Straße des 17. Juni 135, D-10623 Berlin, Germany

³Northeastern University, Department of Electrical and Computer Engineering, 440 Dana Research Building, Boston, MA 02115, USA

(Received 3 May 2007 and in revised form 27 March 2008)

Drag reduction strategies for the turbulent flow around a D-shaped body are examined experimentally and theoretically. A reduced-order vortex model describes the interaction between the shear layer and wake dynamics and guides a path to an efficient feedback control design. The derived feedback controller desynchronizes shear-layer and wake dynamics, thus postponing vortex formation. This actuation is tested in a wind tunnel. The Reynolds number based on the height of the body ranges from 23 000 to 70 000. We achieve a 40% increase in base pressure associated with a 15% drag reduction employing zero-net-mass-flux actuation. Our controller outperforms other approaches based on open-loop forcing and extremum-seeking feedback strategies in terms of drag reduction, adaptivity, and the required actuation energy.

1. Introduction

We experimentally study the effect of open- and closed-loop flow control on the coherent structures in the wake of an elongated D-shaped body. A key enabler for robustness and efficient control design is an understanding of the mechanism of active flow control by analysis of a reduced-order vortex model. This knowledge is utilized to design an efficient control strategy for the reduction of pressure-induced drag. Our focus is on feedback control for wake stabilization leading to drag reduction.

The flow around ground and airborne transport vehicles is determined by aerodynamic design, manifesting a trade-off between fluid-dynamical and practical requirements, such as usability, safety, reliability and cost (Hucho 2002). The discipline of aerodynamic design has become mature, owing particularly to potential theory. Small control devices can subsequently be added to improve performance and widen the dynamical envelope by the manipulation of boundary and shear-layer physics (Leder 1992). Control devices range from passive, active open-loop to active closed-loop actuation. This paper is focused on the latter. These flow control approaches have been explored in the community for decades.

† Author to whom correspondence should be addressed: Mark.Pastoor@TU-Berlin.de

Various passive means for bluff body flow control are well-investigated and have been applied in numerous experiments. For example, Bearman (1965) described the stabilizing effect of a splitter plate on the wake flow. Tanner (1972) examined the drag reduction for various kinds of a spanwise modulation of the trailing edge, such as segmented, curved, and M-shaped trailing edges. A significant drag reduction on a blunt-based model was achieved by modifying vortex shedding using wavy trailing edges or vortex disruptors (Tombazis & Bearman 1997; Park *et al.* 2006).

Passive devices, such as vortex generators, may have an adverse effect, away from the specific operating conditions for which they were designed. Active flow control can reproduce effects of passive devices. In addition, it can widen the operating envelope with beneficial impact by adapting to changing flow conditions. Literature surveys on open-loop flow control are provided by Fiedler & Fernholz (1990) or Gad-el-Hak, Pollard, & Bonnet (1998). For instance, a beneficial effect of active base bleed for drag reduction was observed by Bearman (1967) and Grosche & Meier (2001). An active control application with spanwise distributed forcing at the trailing edges of a two-dimensional bluff body was described by Kim *et al.* (2004). Here, a significant drag reduction and a suppression of vortex shedding in the wake was achieved by open-loop forcing, both in experiment and LES. Another approach is active surface actuation. This strategy was applied to airfoils (Wu, Xie & Wu 2003) in order to increase the aerodynamic performance and for drag reduction of a circular cylinder (Wu, Wang & Wu 2007). The first active open-loop flow control demonstration for a full-scale aeroplane was achieved by Wygnanski (2004) with an XV-15 tilt-rotor aircraft.

Closed-loop flow control offers further degrees of freedom to improve actuation efficiency. It requires mathematical or conceptual models that link actuation effects and sensor information (figure 1). Model and controller have to be selected with respect to the behaviour of the flow.

(a) Model-independent controllers based on gradient methods can be implemented, when this actuator–sensor relationship is characterized by a steady-state map with an extremum.

(b) Transfer functions describe linear input–output relations of actuation signals and sensor readings. They allow for control design based on black-box models.

(c) Coherent structure models enable a nonlinear description of the system dynamics, as made evident in vortex pairing, amplitude saturation, etc. The implementation of optimal control based on such reduced-order models in experiment is a challenge due to the enormous computational load. Physically motivated controllers may require less numerical effort and are enabled by the understanding of the key processes.

Current application of closed-loop flow control mainly concentrates on few well established benchmark problems, such as the control of the flow around a circular cylinder, around a backward-facing step or over a cavity (Cattafesta *et al.* 2003; Collis *et al.* 2004). One of the first implementations of feedback flow control in an experiment is described by Roussopoulos (1993).

Gradient-based model-independent feedback schemes are extremum- and slope-seeking feedback controllers that search for optimal actuation parameters (Henning & King 2005*b*; Beaudoin *et al.* 2006; Henning *et al.* 2007). Extremum-seeking can be used to find distinct minima or maxima in the steady-state map. One example is the adjustment of the height and thus the resonance frequency of a Helmholtz resonator. This actuator may increase the pressure recovery of the detaching diffuser flow (Garwon *et al.* 2003). On the other hand, when the optimal performance is characterized by the crossover from a rising or falling to a saturated parameter

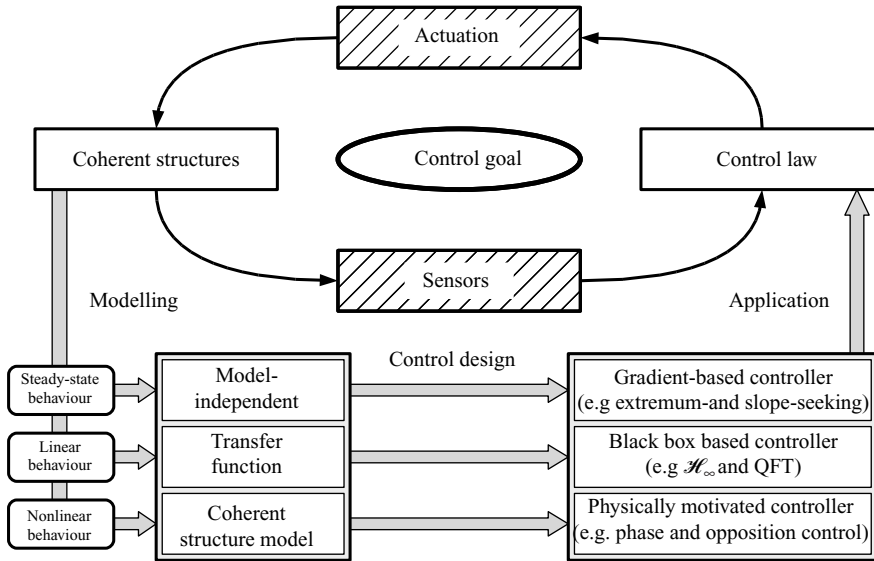


FIGURE 1. The coherent structure dynamics determines the choice of the controller. The structures communicate actuation effects to the sensors, e.g. pressure readings. The control law computes actuation signals from the current state resolved by sensor readings. The actuators manipulate excitable coherent structure dynamics in order to enforce the control goal, here the reduction of drag. A range of feedback flow control schemes allows us to select the best-suited control law, depending on the behaviour of the flow, as elaborated in the text.

regime, slope-seeking feedback is preferred. A case in point is the saturated effect of an actuation amplitude on the separation region and flow reattachment over an aircraft wing (Becker *et al.* 2007). Once the flow is completely attached, further increases in amplitude will not lead to significant changes in the lift.

Control design based on experimentally identified black-box models was conducted by Becker *et al.* (2005), King *et al.* (2004) and Henning & King (2005a). Here, the turbulent reattachment process behind a backward-facing step was controlled at Reynolds numbers up to 25 000 based on the step height. Robust closed-loop control based on these models was able to prescribe the reattachment length and to compensate disturbances. Adaptive schemes were developed by Garwon *et al.* (2003) to adjust the actuation amplitude. Henning *et al.* (2007) proposed a black-box model to control the pressure drag of a D-shaped body at Reynolds numbers based on body height up to 70 000. Rowley *et al.* (2002) suppressed Rossiter modes of a cavity flow by black-box model-based control.

Black-box models, however, do not resolve coherent structures of the flow: they merely link input and output signals. Reduced-order vortex and POD models explicitly describe the coherent structures as communicators between input and output. POD models were employed for flow control of different configurations, e.g. the cylinder wake (Bergmann, Cordier, & Brancher 2005; Gerhard *et al.* 2003; King *et al.* 2005; Noack *et al.* 2003; Noack, Tadmor & Morzyński, 2004; Noack, Papas & Monkewitz, 2005; Tadmor *et al.* 2004; Siegel, Cohen, & McLaughlin 2003; Siegel *et al.* 2007, 2008) or the cavity flow (Little *et al.* 2007). Introductions to POD models are provided by Lumley & Blossey (1998) or Cordier & Bergmann (2003).

POD models are convenient for standard control design, due to their mathematical structure. In contrast, vortex models inhibit most control design methods by their

hybrid nature (changing phase space of vortex positions). However, vortex models exhibit a larger dynamical bandwidth, which is crucial for the current flow control task. The theoretical foundation of vortex models dates back to Helmholtz (1858) and Thomson (1869). In the early twentieth century the N -vortex problem was discussed. Von Kármán (1911) used vortex models for a stability analysis of the vortex street configuration. A numerical simulation of a mixing layer using point vortices was conducted by Rosenhead (1931), encouraging investigations of many configurations until the 1960s. Birkhoff (1962) found an inherent ill-posed convergence behaviour in vortex models. This finding gave rise to doubts about the predictive power of this modelling approach. Nonetheless, vortex models were pursued by several authors, such as Clements (1973), who described vortex shedding in the wake of a bluff body. Later, convergence of vortex models with finite-core radii to solutions of the Navier–Stokes equation could be shown (Beale & Majda 1982; Krasny 1986). In the 1980s and 1990s high-dimensional vortex models were investigated by several researchers (Ghoniem & Gagnon 1987; Cottet & Koumoutsakos 2000; Soteriou 2003) as an alternative approach to DNS, and extended for three-dimensional flows (Leonard 1985; Meiburg 1995). In recent years reduced-order models were proposed as coherent structure models (Cortelezzi 1996; Coller *et al.* 2000) and plants for control design (Tang & Aubry 2000; Protas 2004, 2006). In this study, reduced-order vortex models are used to explain the physical effects of actuation and to improve control. Efficient means to synchronize two-dimensional coherent flow structures for achieving the control goal, a significant drag reduction, are proposed.

This paper is organized as follow. In §2, we describe the experimental setup and the vortex model. Our study and analysis of the natural and open-loop forced flow is detailed in §3. The observed processes are explained in §4. Experiments with feedback controllers are outlined in §5. Finally, we summarize the main findings and their implications for other configurations in §6. The vortex model and the extended Kalman filter used in §5 are detailed in Appendices A and B, respectively.

2. Experimental testbed and vortex model

This section provides a description of the experimental setup and outlines the vortex model.

2.1. Wind tunnel

Experiments are conducted in an Eiffel-type wind tunnel. The maximum free-stream velocity is approximately 20 m s^{-1} with a turbulence level of less than 0.5%. The dimensions of the closed test section are $L_{ts} = 2500 \text{ mm}$, $H_{ts} = 555 \text{ mm}$ and $W_{ts} = 550 \text{ mm}$ in the streamwise, transverse and spanwise directions, respectively. The flow is described in a Cartesian coordinate system x, y, z ; the origin is located at the vertical and horizontal centre of the body's stern (see figure 2).

The D-shaped body has the following dimensions: chord length $L = 262 \text{ mm}$, body height $H = 72 \text{ mm}$ and spanwise width $W = 550 \text{ mm}$. The geometric blockage of the model in the wind tunnel is approximately 13%. Therefore, the free-stream velocity U_∞ is adjusted to $U_{\infty,c} = U_\infty \sqrt{B_c}$, according to the blockage correction method proposed by Mercker (1980). Trip tapes are placed 30 mm downstream of the nose in order to trigger boundary layer transition. The model is mounted on two aluminium rods and is vertically centred in the wind tunnel. The rods have a diameter of 15 mm and are attached to the model's lower surface at $(x, y) = (-131 \text{ mm}, -175 \text{ mm})$ and $(x, y) = (-131 \text{ mm}, 175 \text{ mm})$, respectively. Reynolds and Strouhal numbers are given

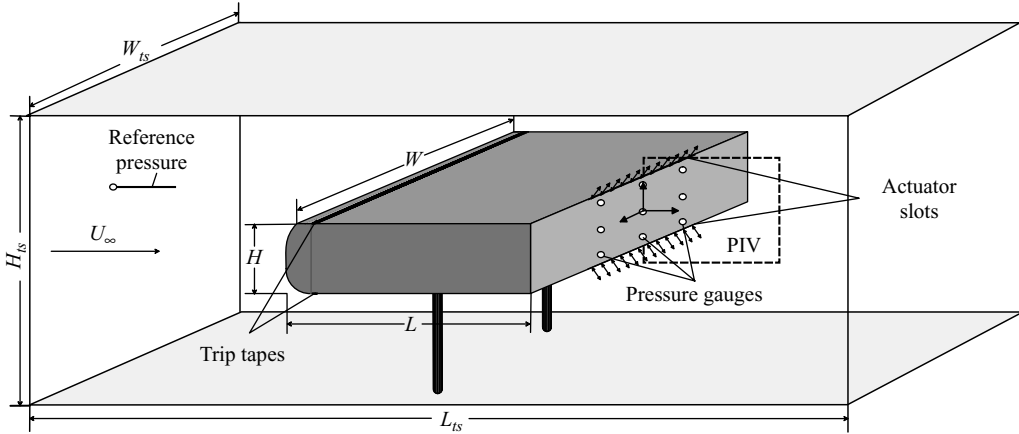


FIGURE 2. Sketch of the experimental setup with the D-shaped body. For details, see text.

with respect to body height and corrected free-stream velocity:

$$Re_H = \frac{U_{\infty,c} H}{\nu} \quad \text{and} \quad St = \frac{f H}{U_{\infty,c}}.$$

Here, ν represents the kinematic viscosity of the fluid and f is the frequency to be expressed as a Strouhal number. All experiments are conducted at Reynolds numbers in the range from 23 000 to 70 000.

A sinusoidal zero-net-mass-flux actuation is effected by loudspeakers (*Visaton W200S*, 4Ω) through spanwise slots (slot width $S=1$ mm, spanwise length 250 mm) located at the upper and lower trailing edges. Harmonic actuation $g(t) = A \sin(2\pi f_A t)$, with the actuation amplitude A and frequency f_A , is applied to each slot, thus generating periodical sucking and blowing. The cost of actuation is characterized by the non-dimensional excitation momentum coefficient

$$c_{\mu} = 2 \frac{S}{H} \frac{q_A^2}{U_{\infty,c}^2},$$

where q_A is the r.m.s. value of the velocity generated by the actuator. The factor 2 accounts for the number of actuators. The actuation signal g is equal to the velocity at the centre of the actuation slot. The frequency response of the actuator is compensated.

The base pressure is monitored by 3×3 difference pressure gauges (*PascaLine PCLA02X5D1*) mounted in three parallel rows on the stern at $y = \{-32, 0, 32\}$ mm and $z = \{-82.5, 0, 82.5\}$ mm. Pressure gauges are calibrated and temperature compensated. Their operating pressure range is ± 2.5 mbar with an accuracy of $\pm 0.25\%$. The free-stream dynamic pressure is monitored by a Prandtl probe. The probe was mounted at $(x, y, z) = (-1181 \text{ mm}, 127.5 \text{ mm}, -175 \text{ mm})$ and is connected to a differential pressure transducer (*MKS Baratron 220D*) with a measurement accuracy of 0.15%. Four strain gauges (*HBM 6/350LY13*, metering precision $\pm 0.35\%$) are applied to the aluminium rods for drag force measurements. The strain gauges are glued on a milled out section of the aluminium rods 5 mm underneath the bluff body. Thereby, the drag on the aluminum rods does not contribute to the measured body force. A power amplifier *HBM ML55b* is used for calibration and voltage

amplification. Base pressure and drag are described by non-dimensional coefficients

$$c_P(y, z, t) = \frac{\Delta p(y, z, t)}{\rho U_{\infty,c}^2/2}, \quad \text{and} \quad c_D(t) = \frac{F_x(t)}{\rho U_{\infty,c}^2 H W/2},$$

respectively. Here, Δp is the instantaneous pressure difference between a stern-mounted pressure gauge and the reference pressure, ρ denotes the density, and F_x is the drag force. Time-averaged base pressure and drag are denoted by $\bar{c}_P(y, z)$ and \bar{c}_D , respectively. The surface-averaged base pressure over the stern is marked by $\langle c_P(t) \rangle$. Boundary layer conditions and velocity fluctuations in the wake flow are acquired by hot-wire measurements, using 5 μm -hot-wires and the constant temperature anemometer *A.A. Lab Systems Ltd. AN-1003*.

PIV measurements are conducted in the vertical symmetry plane ($x \in [0, 144]$ mm, $y \in [-58, 58]$ mm and $z = 0$ mm) at $Re_H = 23\,000$ with a spatial resolution of $dx = dy = 2.3$ mm. Temporal resolution is limited to 4 Hz. The PIV system consists of a frequency-doubled Nd:YAG laser, a CCD-Cross-Correlation-Camera (*PCO SensiCam Double Shutter*) and a synchronization unit. The *VidPiv* software of *ILA corp.* is used for the computation of velocity fields. Data acquisition and the implementation of the controllers is realized by rapid prototyping hardware (*dSPACE-PPC1005* controller). The sampling time is $\Delta t = 1/1000$ s.

2.2. Vortex model

Hereafter, all quantities are non-dimensionalized by H , $U_{\infty,c}$ and ρ . Experimental and numerical investigations show that the initial separation and roll-up of the shear layers in the bluff body wake is dominated by two-dimensional coherent structures (see §3.3). On a kinematic level, two-dimensional vortex models approximate the vorticity distribution ω of the flow by adding vortices to an irrotational flow with the potential Φ (e.g. Milne-Thomson 1968; Lugt 1996). The induced velocity from N vortices at a sample point \mathbf{x} is calculated by

$$\mathbf{u}(\mathbf{x}, t) = \nabla\Phi(\mathbf{x}, t) + \sum_{i=1}^N \Gamma_i \mathbf{u}^\omega(\mathbf{x}, \mathbf{x}_i), \quad (2.1)$$

where Γ_i is the circulation and \mathbf{x}_i the position of the i th vortex. The circulation is constant by Helmholtz's law. The kernel \mathbf{u}^ω is derived from potential theory using Biot-Savart's law for the induced velocity. The vortices move with the flow:

$$\frac{d\mathbf{x}_i}{dt} = \mathbf{u}(\mathbf{x}_i, t), \quad i = 1, \dots, N. \quad (2.2)$$

In this paper, a reduced-order vortex model for the flow around the D-shaped body in a wind tunnel is proposed. Approximately 650 vortices are required to resolve the dynamics of the coherent structures. Similar models have been investigated for the flow around a D-shaped body (Clements 1973), the flow over an edge (Evans & Bloor 1977), the wake flow past a plate (Cortezzi 1996), the diffuser flow (Coller *et al.* 2000), and the flow around a backward-facing step (Pastoor *et al.* 2003). The no-penetration boundary condition at the walls for the potential flow is enforced by using a conformal mapping from the upper half-plane onto the D-shaped body (see §A.1). Boundary conditions are enforced in the computational domain. The potential flow is represented by a pair of sources in the computational domain (see §A.2). The effect of zero-net-mass-flux actuation is modelled by two oscillating sources at the trailing edges of the body (see §A.3). Vortices and their mirror images transform into a vortex solution in the physical domain that respects the no-penetration condition

at the walls (see § A.4). Vortex production at the trailing edges follows a generalized Kutta condition a fair approximation of the production rate, while smoothing the stochastic vorticity production in the boundary layers. In order to maintain the low-dimensionality of the model, vortices are gradually merged (see § A.6), where a high resolution is not required ($x > 2$) or faded out, when they leave the region of interest ($x > 30$). The numerical integration of (2.2) is computed by a third-order, explicit Adams–Bashforth scheme.

3. Investigation of the natural and periodically forced flow

Key features of the natural and the periodically forced (open-loop) flow around the D-shaped body are described in § 3.1 and § 3.2, respectively.

3.1. Natural flow

The flow around the D-shaped body is governed by an absolute wake instability (Huerre & Monkewitz 1990). This mechanism generates a von Kármán vortex street with an alternating sequence of vortices at characteristic frequencies. The two-dimensional vortex shedding in a wake of a bluff body is only weakly perturbed by three-dimensional fluctuation (Zhang *et al.* 1995).

An instantaneous vorticity field of the natural flow at $Re_H = 23\,000$ captured by PIV indicating bent shear layers at the upper and lower edges is shown in figure 3(a). Two large vortical structures appear almost at the centreline, whereas the lower vortex is closer to the stern. Pressure readings indicate a pressure minimum at the bottommost pressure gauges. The time-averaged and spatially averaged base pressure coefficient is $\langle \bar{c}_{p,0} \rangle = -0.53$. This corresponds to an average drag coefficient of $\bar{c}_{D,0} = 0.98$. Dominant Strouhal numbers of bluff body wakes are usually within a range of 0.2 for circular cylinders and 0.26 for short D-shaped bodies (Leder 1992).

In agreement with these common observations, the frequency spectra of hot-wire measurements at $(x, y, z) = (1, 0.7, 0)$ indicate a maximum fluctuation level at $St \approx 0.23$ in the current study. Upper and lower boundary layer conditions, as the boundary layer thickness δ_{99} , the momentum deficit thickness δ_2 and the form factor H_{12} , are acquired by hot-wire measurements in the vicinity of the trailing edges $(x, y, z) = (-0.01, \pm 0.5, 0)$ and averaged. The results are in good agreement with measurements given by Bearman (1967) and Park *et al.* (2006). The large boundary layer thickness observed at $Re_H = 23\,000$ results from a small separation bubble in the front section of the body. This phenomenon was reported by Cooper (1985) for bluff bodies with rounded front edges. The results for the investigated range of Reynolds numbers and the two reference cases are summarized in table 1.

Figure 3(d) displays the vorticity field obtained from a snapshot of the vortex model. The corresponding pressure field can be calculated by solving the Poisson equation:

$$\Delta p = -\nabla \mathbf{u} \cdot \nabla \mathbf{u}^T = \mathbf{W} \cdot \mathbf{W} - \mathbf{S} \cdot \mathbf{S} = Q, \quad (3.1)$$

where $\nabla \mathbf{u}$ is the Jacobian of the velocity, the superscript T denotes the transpose of the tensor and $\cdot \cdot$ is the double contraction. The Jacobian $\nabla \mathbf{u}$ is decomposed in a symmetrical tensor \mathbf{S} and a antimetrical tensor \mathbf{W} . Here, \mathbf{S} represents the strain and \mathbf{W} the rotation of a fluid element. In (3.1), the source term Q can be expressed as the local difference of the double contraction of the rotation and strain tensors, respectively. Inside a vortex, rotation dominates ($Q > 0$), which indicates a lower pressure in the core, according to (3.1). In a plain shear layer, rotation and strain are balanced ($Q = 0$). On the convex side of a bent shear layer and between vortices,

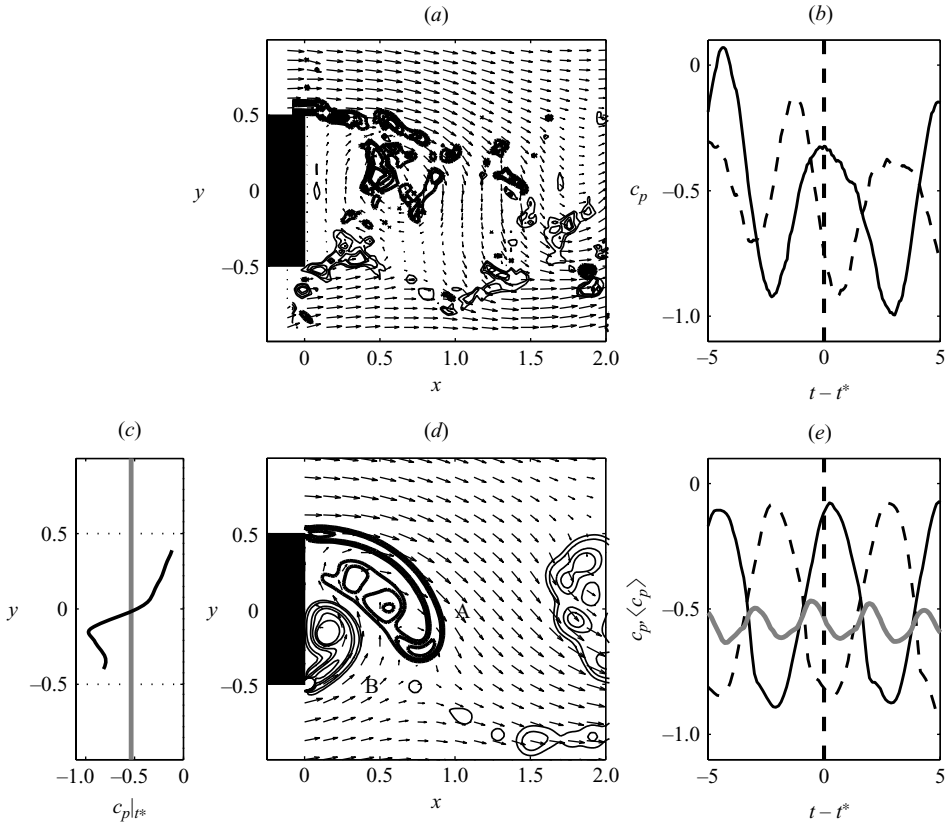


FIGURE 3. Natural flow of the experiment (a,b) and of the vortex model (c–e). Instantaneous flow field of the natural flow at $Re_H = 23000$, captured by PIV (a) and the vortex model (d) at the reference time t^* . The velocity field is indicated by black arrows. The spanwise vorticity component is displayed by isolines $\{\pm 12, \pm 10, \pm 7, \pm 5\}$, where negative (positive) values are indicated by thick (thin) lines. In (b) and (e), respectively, time series of experimentally and numerically obtained pressure readings c_p of the topmost (—) and bottommost (---) sensors at $z = 0$ are displayed. The experimental pressure data are low-pass filtered. The surface-averaged base pressure $\langle c_p \rangle$ (—) is plotted in (e). The pressure distribution $c_p(y)$ (—) and the temporally and spatially averaged base pressure $\langle \bar{c}_p \rangle$ (—) are shown in (c).

The vortex street originates close to the stern. A small separation bubble and strong vortices in the vicinity of the body are responsible for a low base pressure and thus for high drag. Vortices are shed with the frequency $St \approx 0.23$.

strain dominates. A saddle point region is marked by $Q < 0$ and is associated with an excess pressure. Velocities and velocity gradients are rather small in the dead water region. With $Q = 0$, the pressure gradients remain constant, thus the base pressure along the stern is determined by the near-wake pressure field. Hence, vortices in the near wake leave pressure reading footprints.

An important aspect of the instability in the near wake is the strong interdependence of the upper and lower shear layers. Referring to figure 3(d), the vortex at $x = 0.6$, denoted vortex A, is created by a roll-up of the upper shear layer. It subsequently pulls the lower shear layer up and induces the creation of a new vortex, denoted B, at $x = 0.2$. Once vortex B grows and convects downstream, it will trigger the creation of a new vortex, originating from the upper shear layer. Thus, strong vortices alternate

Re_H	δ_{99}	δ_2	H_{12}	$\langle \bar{c}_{P,0} \rangle$	$\bar{c}_{D,0}$	St	B_c
23 000	0.22	0.017	1.19	-0.53	0.89	0.23	1.32
35 000	0.18	0.015	1.19	-0.52	0.92	0.23	1.33
46 000	0.16	0.014	1.21	-0.52	0.89	0.23	1.34
58 000	0.16	0.014	1.21	-0.51	0.90	0.25	1.32
70 000	0.16	0.013	1.20	-0.51	0.91	0.25	1.32
41 000 [†]	0.12	0.017	1.47	-0.57	-	0.24	-
40 000 [‡]	0.22	0.017	-	-0.55	-	0.25	-

[†] Bearman (1967), $H = 25.4$ mm, $x = -0.1$
[‡] Park *et al.* (2006), $H = 60$ mm, $x = -0.033$

TABLE 1. Base flow parameters of the experiment and similar studies of Bearman (1967) and Park *et al.* (2006). For details, see text.

in the near wake, yielding a short dead water region and strongly bent shear layers. As explained above, this results in low pressure at the base and a high drag. The current base pressure distribution $c_p(y, t^*)$ in figure 3(c) displays the asymmetrical shedding of vortices. The creation of vortex B is visible by its footprint in the base pressure.

3.2. Periodical forcing

The sensitivity of the flow to open-loop forcing was investigated experimentally for a wide range of Reynolds numbers, actuation frequencies and amplitudes. Upper and lower actuators were operated both in-phase and anti-phase, but anti-phase operation is unsuitable to reduce drag efficiently.

Averaged base pressure and drag coefficients are plotted in figure 4(a, b) against the Strouhal number of the actuation. Actuators operate in-phase with a constant amplitude $c_\mu = 0.01$, which corresponds to a maximal velocity equal to the free-stream velocity. Both coefficients are normalized by the base pressure and drag coefficient of the natural flow, respectively. There is a maximum base pressure at $St_A \approx 0.15$ for all studied Reynolds numbers, which yields a drag reduction of almost 15%. No beneficial modification of the base pressure is observable for Strouhal numbers below $St_A = 0.05$ and above $St_A = 0.3$. Experiments were performed with Strouhal numbers up to $St_A = 3.5$. There is a striking collapse of the pressure in a small band centred at the Strouhal number of the wake instability ($St_W \approx 0.23$). Here, the drag is increased above the level of the natural flow.

Figure 4(c, d) illustrates the effect of different actuation amplitudes on the average base pressure and drag for the most efficient Strouhal number $St_A = 0.15$. Obviously, there are Reynolds-number-dependent bounds on c_μ before forcing significantly increases the base pressure. Above a certain amplitude, the pressure runs into a saturation level of $\langle \bar{c}_P \rangle / |\langle \bar{c}_{P,0} \rangle| = -0.6$. At $Re_H = 46\,000$ these asymptotic values are $c_\mu^{\min} \approx 0.0025$ and $c_\mu^{\max} \approx 0.006$, respectively. In the intermediate regime, the natural and saturation levels are almost linearly connected. The drag coefficient shows a similar behaviour.

The effects of actuation with $St_A = 0.15$ and $c_\mu = 0.009$ at $Re_H = 23\,000$ are illustrated in figure 5 by instantaneous vorticity fields obtained from PIV and the vortex model. The shedding of vortices from the upper and lower edges occurs synchronously, as indicated by the flat base pressure distribution $c_p(y, t)$. The first two vortices appear at a greater distance to the stern compared to the natural flow.

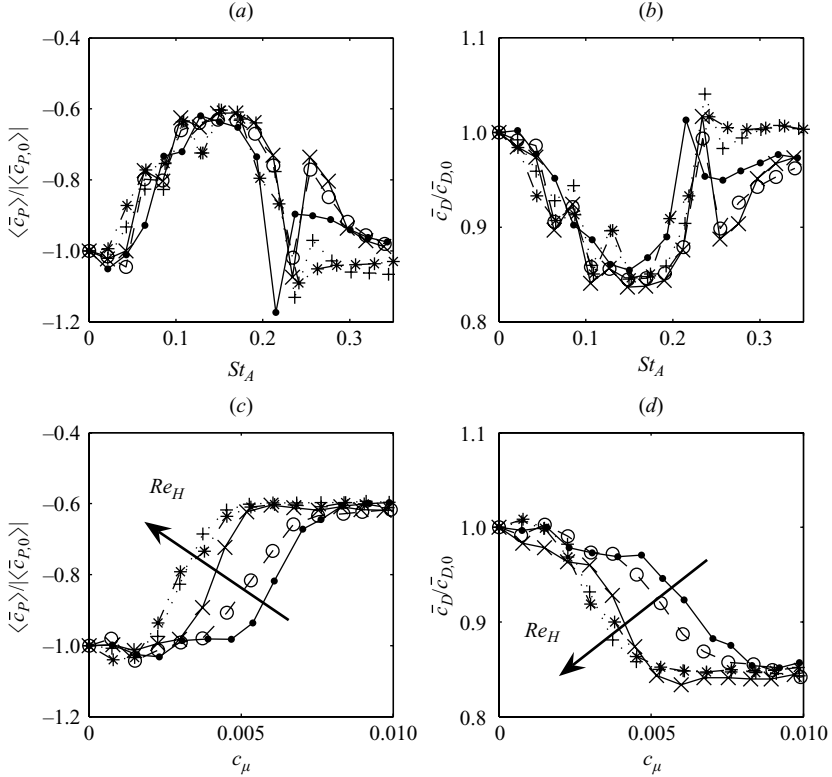


FIGURE 4. Normalized and averaged base pressure (*a,c*) and drag coefficient (*b,d*). These parameters are plotted as functions of the actuation frequency St_A at $c_\mu = 0.01$ (*a,b*), and as functions of the momentum coefficients (*c,d*) at $St_A = 0.15$ and Reynolds numbers 23 000 (\bullet), 35 000 (\circ), 46 000 (\times), 58 000 ($+$), 70 000 ($*$).

As a result, the formation of the alternating vortex street is delayed and the dead water region is elongated. The mean base pressure increases by 40% while the drag decreases by 15%.

The net power saving due to the actuation effect is determined in what follows. The towing power reduction $\Delta\mathcal{P}_D$ is computed by

$$\Delta\mathcal{P}_D = U_{\infty,c} \Delta\bar{F}_x. \quad (3.2)$$

Here, $\Delta\bar{F}_x$ denotes the time-averaged reduction of the drag force. The electrical power \mathcal{P}_{el} of each actuator is

$$\mathcal{P}_{el} = \mathcal{U}_{eff} \mathcal{I}_{eff} \cos \varphi, \quad (3.3)$$

where \mathcal{U}_{eff} and \mathcal{I}_{eff} are, respectively, the effective voltage and current applied to the actuator, and φ is the phase between both. A gain $|\Delta\mathcal{P}_D|/2\mathcal{P}_{el} > 1$ implies a net saving. The electrical power requirement for in-phase forcing with the most efficient frequency $St_A = 0.15$ and the achieved drag reduction are summarized in table 2 for the investigated range of Reynolds numbers. We find a gain of 2.4 to 2.8 for periodical forcing.

3.3. Two-dimensional flow characteristics

In this section the two-dimensionality of the flow under nominally two-dimensional boundary conditions is investigated. Simultaneous hot-wire measurements at $x = 1$

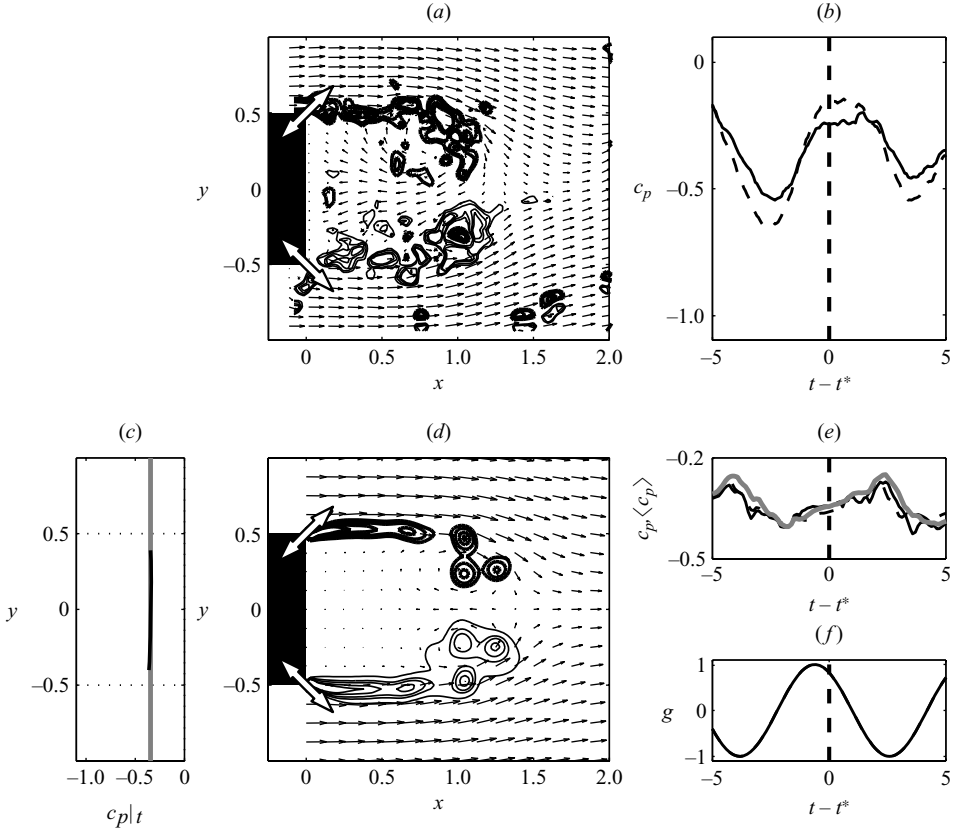


FIGURE 5. The same as figure 3, but for the open-loop forced flow at $St_A = 0.15$ and $c_\mu = 0.009$. The actuation signal g is plotted in (f). Both plots (a) and (d) reveal a symmetrized vortex formation, while the formation of the vortex street is delayed. Vortices shed with the actuation frequency. Base pressure increases by 40% and drag decreases by 15% compared to the natural flow. Actuation signal and topmost and bottommost pressure readings, respectively, have a phase difference of approximately 180° .

Re_H	c_μ	$\Delta \bar{F}_x$ [N]	ΔP_D [W]	\mathcal{U}_{eff} [V]	\mathcal{I}_{eff} [A]	φ [deg.]	\mathcal{P}_{el} [W]	$ \Delta \mathcal{P}_D /2\mathcal{P}_{el}$
23 000	0.009	-0.087	-0.482	0.741	0.127	5.0	0.094	2.6
35 000	0.008	-0.186	-1.554	1.405	0.210	7.0	0.293	2.6
46 000	0.007	-0.325	-3.669	2.514	0.285	8.0	0.710	2.6
58 000	0.006	-0.504	-6.996	3.921	0.322	9.0	1.247	2.8
70 000	0.005	-0.732	-12.1454	5.839	0.436	8.0	2.520	2.4

TABLE 2. Electrical power supply of the actuators (\mathcal{P}_{el}) and the saved power ($\Delta \mathcal{P}_D$) due to open-loop forcing at $St_A = 0.15$. For details, see text.

and $y = \pm 0.7$ are conducted with three probes at $z = \{-1.15, 0, +1.15\}$ and $z = \{-1.74, 0, +1.74\}$, respectively. Velocity fluctuations of the natural flow at $Re_H = 46000$ are plotted in figure 6(a,b). The velocity fluctuations are found to be governed by large eddies in the wake. Spanwise variations, especially the phase differences, are small. This is an indicator for mainly two-dimensional characteristics of the coherent structures.

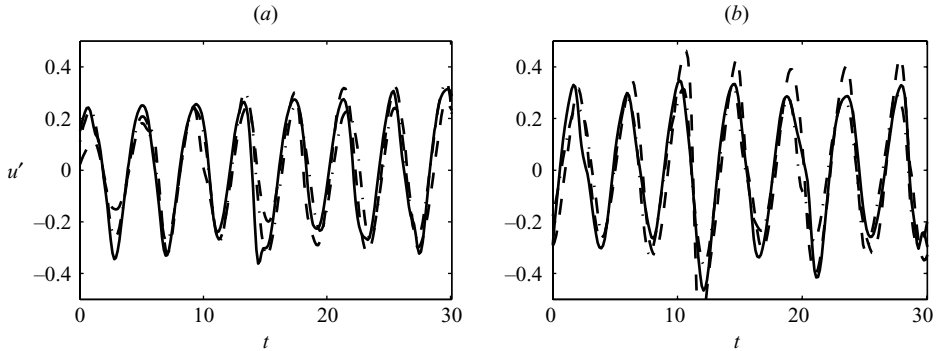


FIGURE 6. Two-dimensional characteristics of the natural flow at $Re_H = 46000$ are demonstrated by the time series of the velocity fluctuations in the wake at $x = 1$ and $y = +0.7$ (a) and $y = -0.7$ (b), respectively. The three hot-wire probes were used simultaneously at $z = -1.74$ (---), $z = 0$ (—) and $z = +1.74$ (-·-).

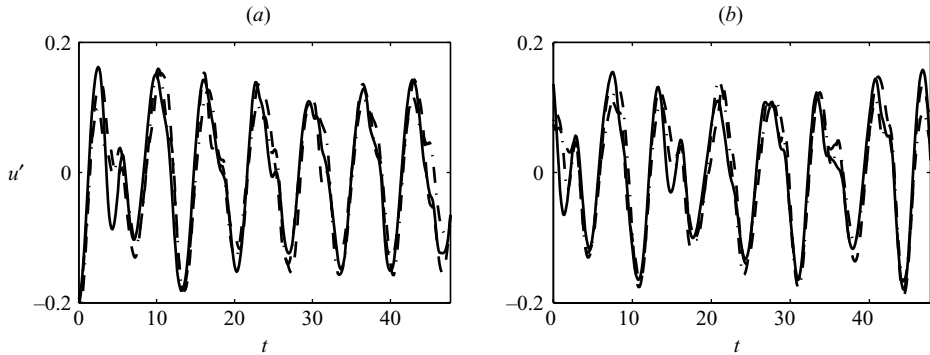


FIGURE 7. The same as figure 6, but for the open-loop forced flow at $St_A = 0.15$ and $c_\mu = 0.007$.

The time series displayed in figure 7(a, b) for the open-loop forced flow at $St_A = 0.15$ and $c_\mu = 0.007$ reveal that actuation does not alter the two-dimensionality of the dominant flow characteristics.

A quantitative investigation is conducted by a Fourier decomposition of the time series. The phase of the leading harmonic is computed to calculate the phase difference between time series obtained at the spanwise centre ($z = 0$) and the four spanwise displaced positions. At $Re_H = 46000$ the phase difference is in the range of -0.4° to 1.2° for the natural flow and -5.7° to 0.4° for the open-loop forced flow. A detailed summary of the results is provided in table 3 in Appendix C.

4. Analysis and modelling for feedback control

In order to improve control, we have to understand how the coherent structures affect the drag, and the way control manipulates these structures. These aspects are discussed in the following. Under open-loop control two-dimensional actuation tends to suppress spanwise variations of the flow structures (Detemple-Laake & Eckelmann 1989). Under closed-loop conditions with sensors in a transverse plane, the appearance of unintended and detrimental three-dimensional features is reported by Seidel *et al.* (2006). In contrast to their investigation of an oscillating cylinder at low Reynolds

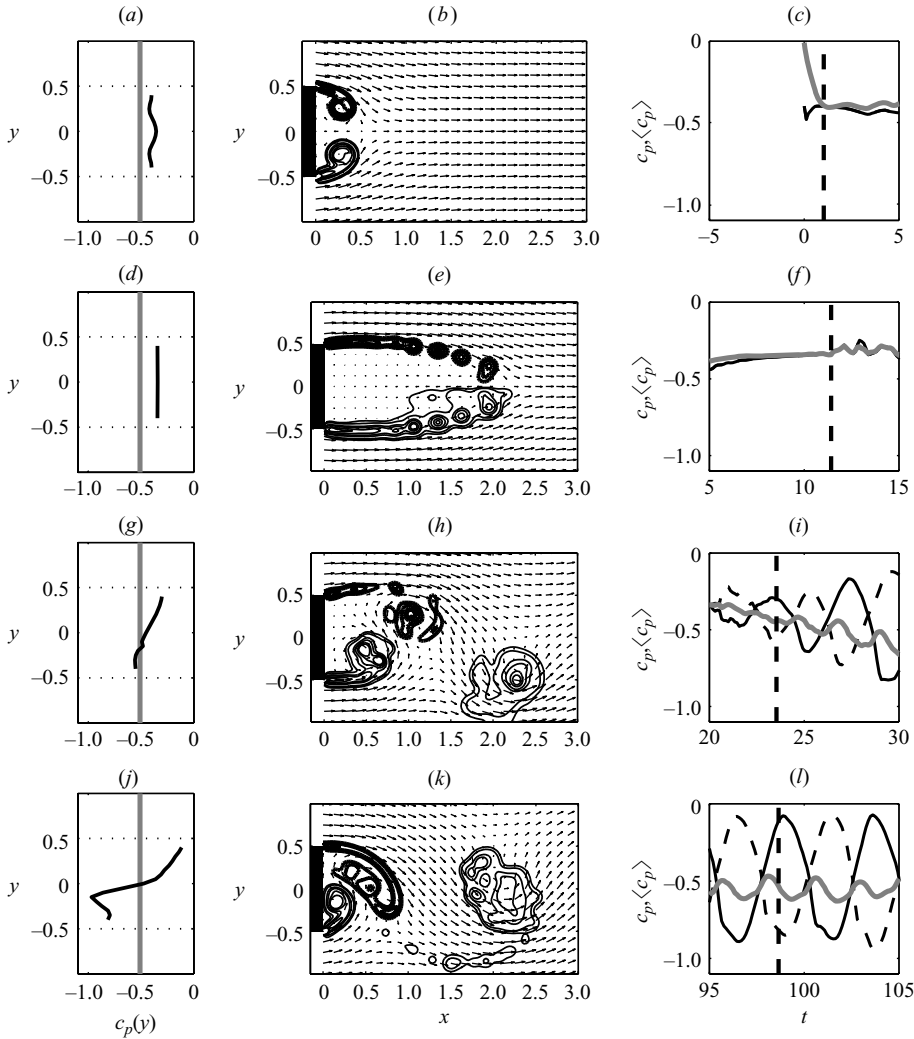


FIGURE 8. Vorticity distribution and base pressure derived from the vortex model illustrating the transient behaviour of coherent structures in the wake. The vortex model simulation starts with the potential solution at $t = 0$. Subsequent stages are: (a–c) startup vortices at $t = 1$, (d–f) almost independent shear layers at $t = 11.5$, (g–i) early interaction (wake instability) at $t = 23.5$ and (j–l) periodical wake at $t = 98.5$. The flow state is depicted as in figure 3(c–e).

numbers (see also Siegel 2007), the feedback actuated flow structures relevant of the D-shaped body wake remain predominantly two-dimensional (as outlined in §3). This can be linked to the fixed separation points at the trailing edges and the turbulent regime of the investigation. Thus, a two-dimensional vortex model is used to explain the spatial development of the wake. The transient development starting from the potential flow inspired our employed feedback controller. As seen in figure 8, one observes four distinct states in the evolution of the wake:

(a) *Startup vortices.* The fluid starts to move and separates at both trailing edges. The shear layers roll up into almost symmetrical vortices. The base pressure distribution is symmetrical as well. These startup vortices convect downstream and eventually dissipate.

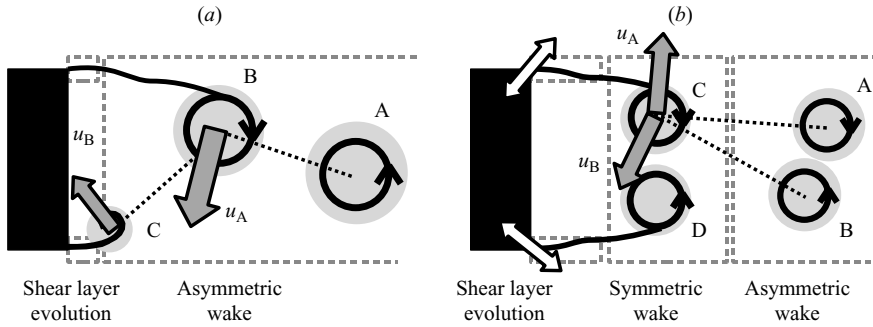


FIGURE 9. Sketch of the coupling between wake and shear layer vortices of the natural flow (a) and the decoupling due to actuation (b). In (a), vortex A triggers the roll-up of the upper shear layer to a vortex B, by inducing the downward velocity u_A . This lumping of vorticity (B) has an impact on the lower shear layer as well. The roll-up of vortex C close to the lower edge is initiated by the induced velocity u_B . A decoupling of wake and shear layer processes is achieved by actuation at the trailing edges (b). By synchronizing the phasing of vortices in the upper and lower shear layers, the appearance of asymmetries is delayed. The induced velocities u_A and u_B of the vortices A and B on vortex C almost annihilate each other. The same is true for vortex D. Thus the wake instability is mitigated.

(b) *Shear layer vortices.* Shear layers are sensitive to free-stream disturbances. Due to convective Kelvin–Helmholtz-type instabilities, these disturbances are amplified in the streamwise direction, hence shear layer vortices evolve. Since the characteristic frequency of this process scales with the shear layer thickness, it is one magnitude above the characteristic frequency of the fully developed wake. Thus, shear layer vortices in this phase are rather weak, because only small portions of vorticity are lumped in each vortex. Further downstream, the small vortical structures may roll up to stronger vortices due to vortex pairing. The base pressure distribution is still almost symmetrical.

(c) *Wake instability.* At this time, the interaction between upper and lower shear layer vortices starts. Any perturbation of the symmetry between upper and lower vortex configuration is amplified. Vortices in the far wake are aligned in an alternating order with a stretched spatial wavelength. The wake instability locks on to large vortical structures. Thus, the alternating sequence of vortices in the far wake has an impact even on upstream processes, in agreement to the implications of an absolute instability. The free-stream disturbances are outpaced by nearly periodic perturbations induced by far-wake vortices. These vortices trigger an alternating shedding of larger vortices in the near wake. The average base pressure declines, while the instantaneous base pressure becomes increasingly asymmetrical.

(d) *Vortex street.* Mutual interaction of both shear layers intensifies alternating shedding (figure 9a). The dead water region decreases. A fully developed vortex street appears rather close to the stern as described in § 3.1. The transition time depends on the initial level of asymmetries. The average base pressure has reached its minimum.

In order to increase the base pressure and reduce the drag, the dead water region has to be elongated and the alternating character of the wake has to be mitigated or delayed. From the control perspective, the suppression of the wake instability is the enabler to increase pressure. There are at least four possibilities to suppress or delay the wake instability by active means:

(a) direct opposition control of vortices in the near wake;

- (b) mitigating the evolution of large-scale vortex formations by high-frequency forcing;
- (c) breaking large-scale vortex formations by forcing three-dimensional structures;
- (d) enhancing the initial symmetry by forcing synchronous vortex shedding.

In search of a tunable and low-cost active control device for existing bluff bodies, we select the last method in the course of this paper. Zero-net-mass-flux actuation increases the magnitude of perturbations in the initial shear layer. The convective instability, which yields shear layer vortices due to roll-up, starts with a larger initial amplitude. From analysis of vortex models of various configurations (mixing layer, backward-facing step, D-shaped body), we know that actuators also command the phasing of vortex roll-up. Transferring this behaviour to our control goal, synchronization of the upper and lower shear layers should be achieved by enforcing in-phase vortex generation. Perturbations of the symmetry would be reduced and therefore the evolution of the wake instability could be delayed. However, in the far wake the alternating character imposed by the wake instability is still a pronounced feature (figure 9*b*).

The effect of actuation on the phase difference between the vortices in the two shear layers is analysed by the phase angles between the actuation signal $g(t)$ and pressure fluctuations $c_p(y, z, t)$ close to the upper and lower edges. The vortex model predicts a phase angle of 180° for optimal open-loop forcing ($St_A = 0.15$). Notwithstanding stochastic short-term effects, pressure fluctuations are also strongly dominated by oscillations at the actuation frequency. A detailed examination of these predictions in experimental results is given in the following.

Phase angles $\Delta\phi_{u/l} = \angle \{g(t)_{u/l}, c_p(\pm 0.44, z, t)\}$, calculated either with pressure readings at the upper or lower edge, are displayed in figure 10(*a, b*) as functions of the Strouhal number of actuation (open-loop). Additionally, these pressure readings are processed by harmonic analysis. We are interested in the amplitudes

$$P(St) = \frac{2}{N_s} \left| \sum_{k=1}^{N_s} c_p(y = \pm 0.44, z = 0, t_k) e^{i2\pi St t_k} \right| \quad (4.1)$$

of harmonic oscillations with the actuation frequency $St = St_A$ as well as the wake instability frequency $St = St_W = 0.23$. Here, N_s is the number of samples. The imaginary unit is denoted by i . The amplitudes $P(St)$ are normalized by the r.m.s. value of the pressure readings and plotted versus the actuation frequency in figure 10(*c, d*).

Four ranges of actuation frequencies are examined in detail: see the frequency ranges (i)–(iv) in figure 4(*a*). In all cases, the Reynolds number is 46 000 and both actuators operate in-phase at a constant actuation amplitude $c_\mu = 0.01$.

Forcing frequencies in the range $0.1 \leq St_A \leq 0.2$ (ii) yield a high base pressure (figure 4*a*). Vortex creation in the upper and lower shear layer occur simultaneously, as indicated by almost identical phase angles between the actuation signal and pressure readings in figure 10(*a, b*). Both phase angles $\phi_{u/l}$ are approximately 170° , which is in accordance with 180° predicted by the vortex model. This figure implies that vortices appear when the actuators switch from blowing to sucking.

Most of the pressure fluctuations are imposed by vortices shed at the actuation frequency, as can be seen by $P(St_A)$ in figure 10(*c*). The influence of the wake instability on the pressure fluctuations is low, as indicated by $P(St_W)$ in figure 10(*d*). Actuation in this frequency range is beneficial, since it triggers strong and synchronized coherent structures in both shear layers. This allows for the evolution of an elongated dead

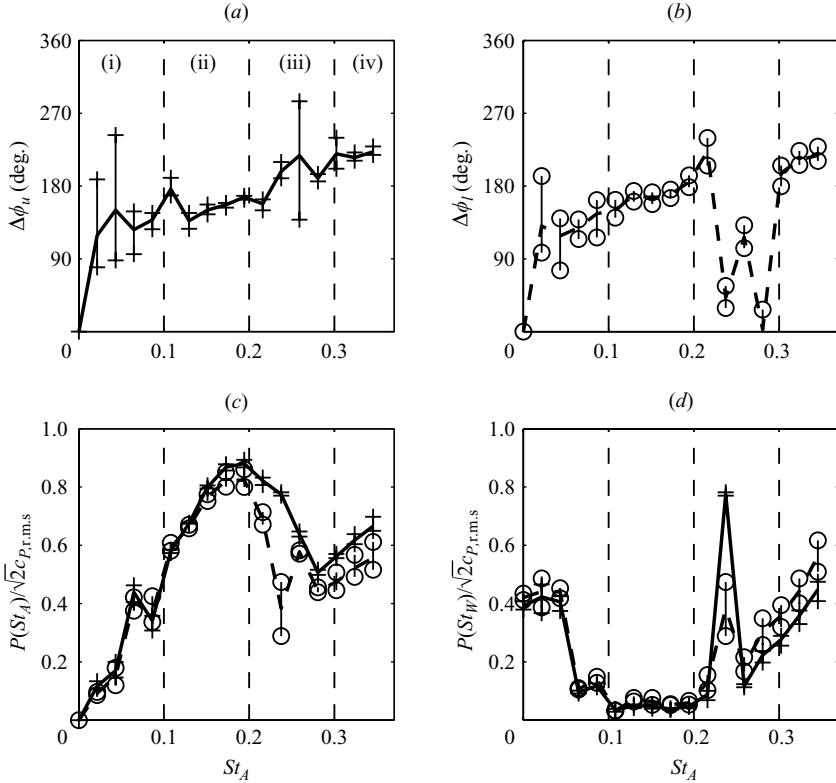


FIGURE 10. Phase and frequency locking of the shear layers due to open-loop control in terms of the Strouhal number at $Re_H = 46\,000$ and $c_\mu = 0.01$. Phase angles between the actuation signal and pressure readings are plotted for actuators and pressure gauges at the upper (—) and lower (---) edges in (a) and (b), respectively. In each case, the results of the three spanwise arranged pressure sensors (see figure 2) are averaged (curve). The vertical lines terminated by + (actuation at upper edge) and \circ (actuation at lower edge) indicate the range of minimum and maximum values. In (c) and (d), the normalized amplitudes $P(St_A)$ and $P(St_W)$ of harmonic projections of the pressure readings (upper edge —; lower edge ---) on the actuation frequency and on the wake instability frequency, respectively, are plotted.

water region. Both shear layers exhibit frequency and phase locking. There is a minimum amplitude required to enforce this phasing (see figure 4c).

There is a lower limit to actuation frequencies, where forcing has no beneficial effect. Below $St_A = 0.1$ (i), phasing between upper and lower vortices differs as ϕ_u and ϕ_l diverge, hence synchronization is poor (figure 10a, b). Moreover, the sensitivity of the shear layers for low-frequency forcing is small. Therefore, $P(St_A)$ decreases and $P(St_W)$ increases (figure 10c, d). In other words, the locking effect decays at low actuation frequencies.

The experiments presented above indicate a pronounced minimum of the base pressure below the unactuated value, when forcing the frequency of the wake instability at $St_A = St_W = 0.23$ (iii). In this frequency range, the phase relation between actuation and pressure readings is different for upper and lower sensors (figure 10a, b). Despite forcing in-phase, the phasing of vortices, as indicated by ϕ_u and ϕ_l , in the upper and lower shear layer is anti-phase and asymmetries are pronounced. Thus, the authority of the actuators to command the phasing of vortex shedding is poor in

this regime. Apparently, the perturbations imposed by the wake instability outpace the attempt to synchronize the shear layer evolution. In fact, the actuators increase the perturbation level of the shear layer in a frequency range that is perfectly suited to amplifying the wake instability. As a result, the base pressure is decreased by 10% whilst drag is increased by some 5% (figure 4*a, b*).

Frequencies in the range $St_A > 0.3$ (iv) are beneficial with respect to base pressure and drag but this effect declines at higher frequencies (figure 4*a, b*). At high frequencies, there is still some authority to command phasing, as vortices are released synchronously (compare ϕ_u and ϕ_l), but fluctuations imposed by these vortices and the wake instability are almost of equal size, as can be seen by comparing $P(St_A)$ and $P(St_w)$ (figure 10*c, d*). High-frequency forcing creates small vortices. Due to roll-up and vortex pairing triggered by the wake instability in the far wake, large alternating coherent structures still appear relatively close to the stern, which reduce the base pressure.

5. Feedback control

As derived in the previous section, our feedback control should decouple shear layer development and wake processes. Increasing the initial symmetry of the flow mitigates the wake instability. This is achieved by forcing a symmetrical vortex formation in the near wake due to a synchronized development of both shear layers. In § 5.1, an adaptive controller is proposed that respects these requirements and finds optimal actuation parameters. A physically motivated controller that explicitly forces a symmetrical evolution of the shear layers is outlined in § 5.2. In both cases, control is applied to the steady-state base flow.

5.1. Adaptive controller

Slope-seeking feedback is an adaptive method for the control of nonlinear plants. It is an extension to well-known extremum-seeking schemes and is described in detail by Krstić & Wang (2000) and Ariyur & Krstić (2003). In § 5.1.1, a slope-seeking feedback scheme for maintaining the optimal actuation amplitude is outlined. Experimental results are presented in § 5.1.2.

5.1.1. Slope-seeking feedback scheme

A block diagram of the slope-seeking feedback scheme is displayed in figure 11. The plant is considered as a block with the input variable $c_\mu(t)$, being the actuation amplitude, and the output variable $\langle c_P(t) \rangle$, represented by the controlled base pressure. We assume that the plant can be described by two characteristic features:

- (1) a plateau-type steady-state input-output map $\langle \bar{c}_P \rangle = m(c_\mu)$;
- (2) a state-space model representing the dynamics of the controlled process.

The control idea is to achieve a state of the plant which is marked by a certain reference slope $m'_{ref} = \partial \langle \bar{c}_P \rangle / \partial c_\mu$ in the steady-state map. Side constraints for this kind of feedback are fast process dynamics in comparison to variations of the input. Neither the dynamical model nor the steady-state map need to be known.

The controller consists of a high-pass and low-pass filter, an integrator, a proportional element with the gain k , and a sine generator. The control input $c_\mu(t)$ is calculated by adding the adaptively computed correction term $\Delta c_\mu(t)$ to the initial control input $c_{\mu,0}$ and superimposing a sine signal with a small amplitude a and the frequency $\omega_{\sin} = 2\pi St$. Thus, the applied actuation signal is

$$c_\mu(t) = c_{\mu,0} + a \sin(\omega_{\sin} t) + \Delta c_\mu(t). \quad (5.1)$$

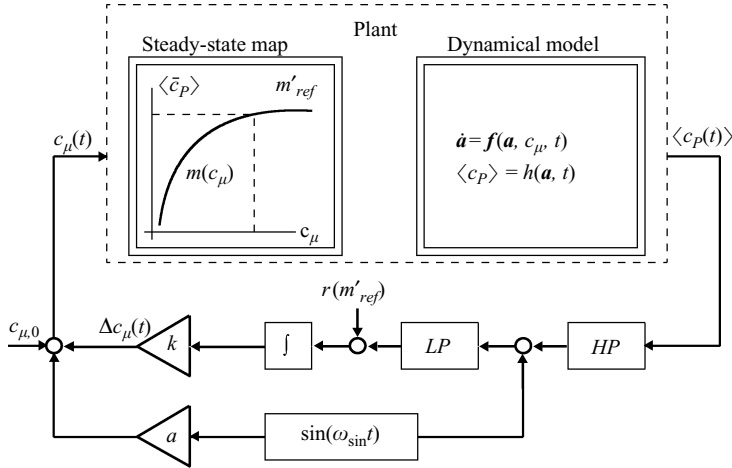


FIGURE 11. Block diagram of the slope-seeking feedback scheme consisting of the plant, a high-pass (HP) and low-pass (LP) filter, an integrator (\int) and a proportional gain (k). The existence of a steady-state map is a prerequisite of this method, whereas the explicit knowledge of $\langle \bar{c}_P \rangle = m(c_\mu)$ and the dynamical model is not needed. For more details, see text.

If the period length of the harmonic perturbation is larger than the largest time constant of the dynamic plant, an almost sinusoidal output $\langle c_P(t) \rangle$ will be obtained, initially centred at $\langle \bar{c}_P \rangle_0 = m(c_{\mu,0})$. This output perturbation is analysed in order to detect the slope of the input–output map and then used for gradient-based optimization. The mean value (initially $\langle \bar{c}_P \rangle_0$) is removed by the high-pass filter. The product of the filtered output and the zero-mean sine signal $\sin(\omega_{\text{sin}} t)$ indicates the local slope $m'(c_\mu)$ of the unknown map. It leads to a non-zero-mean signal obtained by the low-pass filter as long as the plateau is not obtained. If $m'(c_\mu)$ is larger than m'_{ref} , the input signal $c_\mu(t)$ has to be increased. To calculate the difference between the current m' and the reference, m'_{ref} , the effect of the high-pass filter has to be accounted for, with an appropriate amplitude and phase correction. This is done by subtracting the output of the low-pass filter from the filtered reference

$$r(m'_{\text{ref}}) = -\frac{a m'_{\text{ref}}}{2} \text{Re} \left\{ \frac{i \omega}{i \omega + \omega_{\text{HP}}} \right\}, \quad (5.2)$$

instead of subtracting it from m'_{ref} itself. Here, $\text{Re}\{ \}$ denotes the real part of a complex value. If this difference is positive, the integrator will increase its output, which after multiplication by k leads to an increased value of $\Delta c_\mu(t)$. The cutoff frequency of the high-pass filter is ω_{HP} .

The slope-seeking scheme is an adaptive closed-loop type of controller that guarantees closed-loop stability if designed properly. The speed of convergence is determined by the choice of certain design parameters, as the gain k , the cutoff frequencies of the high-pass and low-pass filter, the amplitude a and the frequency ω_{sin} of the sine signal. Cut-off frequencies of the high-pass and low-pass filter need to be lower than the frequency of the perturbation signal. In addition, the gain k needs to be small. The overall feedback system has a fast, a medium and a slow time scale corresponding to the dynamics of the plant, the periodic perturbation and the filters in the slope-seeking scheme, respectively. If the characteristic time scale of the plant varies due to uncertainties, the time scales of the perturbation signal and the

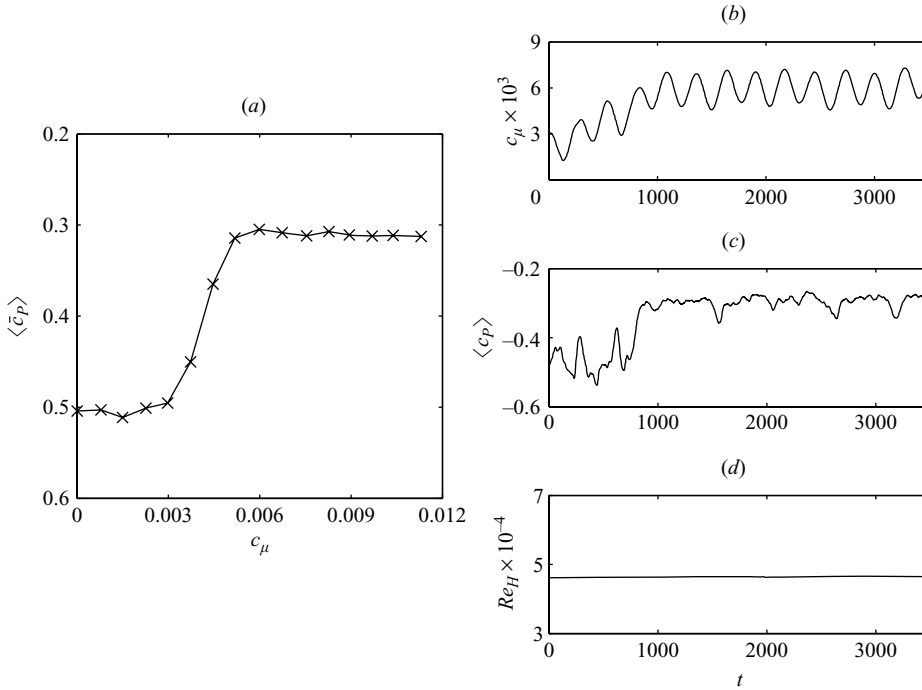


FIGURE 12. Steady-state map $\langle \bar{c}_p \rangle = f(c_\mu)$ obtained from open-loop experiments (a) and experimental implementation of slope-seeking feedback (b–d). The controller adapts the actuation amplitude (b), until the saturation level of the base pressure (c) has been reached. The Reynolds number is 46000 (d). The actuation frequency is fixed at $St_A = 0.15$.

filters have to be slower than the slowest time scale of the plant's dynamics. The main advantage of slope-seeking control, that no *dynamic* model of the plant is required for controller synthesis, is enabled by permanent harmonic perturbations of input and output signals.

In the present study, the momentum coefficient $c_\mu(t)$ is chosen as the input variable, and the output is given by the spatially averaged base pressure coefficient $\langle c_p(t) \rangle$. For the experiments the parameters of the slope-seeking controller have been selected appropriately. The cutoff frequencies of both the high-pass and low-pass filter are set to $\omega_{HP} = \omega_{LP} = 2\pi St_A/40$. The frequency of the sine signal is equal to the cutoff frequencies of the filters, while for the amplitude $a = 1.1 \times 10^{-3}$ is selected.

5.1.2. Experimental results of slope-seeking feedback

Figure 12(a) illustrates the steady-state map with the mean base pressure coefficient as a function of the momentum coefficient at a constant Reynolds number 46000 obtained from the open-loop experiments. This steady-state map is characterized by a plateau at $c_\mu \geq 6 \times 10^{-3}$. The control goal is to find the maximum pressure where the least control input is necessary. This condition is considered as being satisfied when $m'_{ref} < 5$.

Experimental data for a single operating condition are illustrated in figure 12(b–d). The controller starts at $c_\mu = 1.9 \times 10^{-3}$. Sinusoidal modifications of c_μ are applied to obtain the local slope. According to the gradient, the actuation amplitude is raised until the crossover to the plateau has been reached. This leads to a significant increase of the base pressure coefficient as shown in figure 12(c), corresponding to the

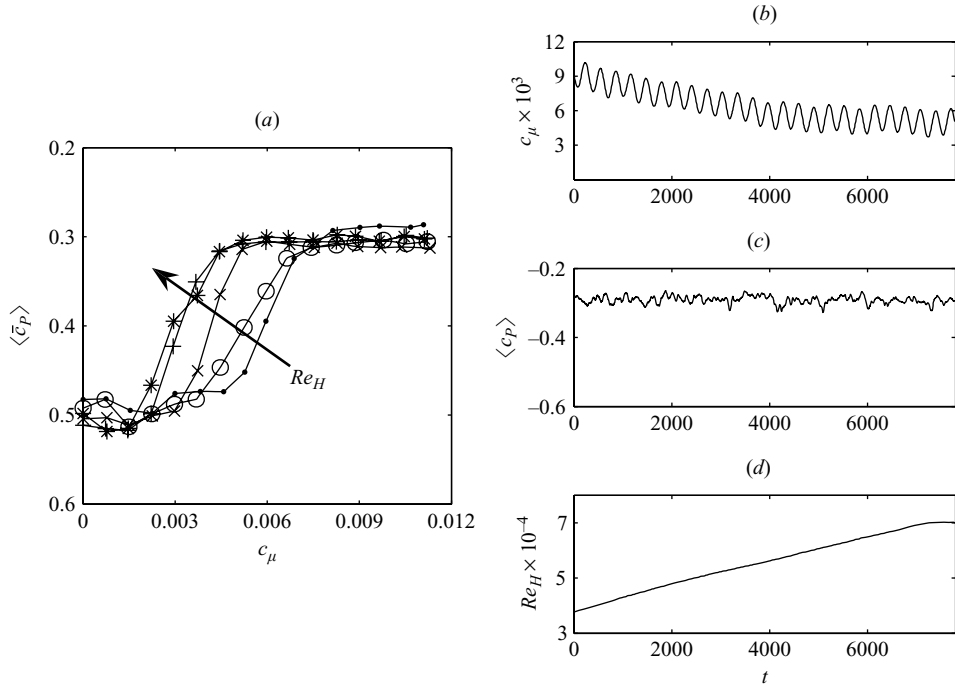


FIGURE 13. The same as figure 12, but for slope-seeking feedback in experiment at Reynolds numbers increasing with time (d). In (a), steady-state maps $\langle \bar{c}_p \rangle = m(c_\mu)$ are displayed at various Reynolds numbers 23 000 (\bullet), 35 000 (\circ), 46 000 (\times), 58 000 ($+$), 70 000 ($*$). These maps are used only to indicate the success of control: they are not required for the controller. The actuation frequency is fixed at $St_A = 0.15$. In (b – d), time is normalized by the oncoming velocity associated with $Re_H = 46\,000$.

steady-state map. In this experiment, the reduction of the drag coefficient by 15%, which has been observed for open-loop forcing, is repeated.

The advantage of slope-seeking feedback is its ability to take into account changing operation points. This property is elucidated by a variation of the Reynolds number, which is increased continuously from 40 500 up to 70 000 (figure 13 d). The steady-state maps for various Reynolds numbers are displayed in figure 13(a). The optimal actuation amplitude decreases with increasing Reynolds number. The experimental results in figure 13(b, c) indicate that the desired averaged base pressure $\langle \bar{c}_p \rangle = -0.3$ is maintained with the minimum control input.

5.2. Phase control for shear layer synchronization

A beneficial effect with respect to drag reduction is achieved by open-loop control and its adaptive, slope-seeking variant, when actuation parameters are selected in order to synchronize upper and lower shear layer development. Both strategies rely on a lock-in mechanism, enforced by the strong effect of symmetric actuation, at both the upper and lower edges of the bluff body. In contrast, the focus of the strategy outlined in § 5.2.1 is on the estimation, explicit utilization and manipulation of the phase of the shear layer periodicity. As will be seen in § 5.2.2, this leads to equal or superior performance, with only a single actuator, translating to a reduction in the actuation power requirement.

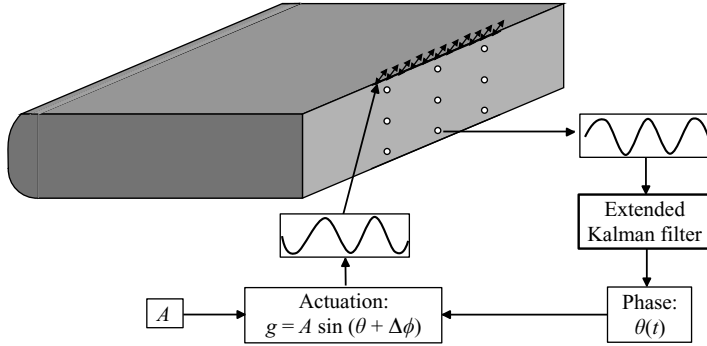


FIGURE 14. Sketch of a single actuator configuration implementing the proposed phase controller. The estimated phase of the pressure oscillations at the lower edge is utilized to calculate the actuation signal, which is applied to the upper actuator.

5.2.1. Implementation of phase control

The guiding principle of the phase feedback is illustrated in figure 14. The pressure fluctuations induced by vortex shedding at the lower edge of the body are monitored at $x=0$, $y=-0.4$, $z=0$. These pressure fluctuations are approximated by a simple sine function $\hat{c}_p(t) = \hat{c}_0 + \hat{c}_1 \sin \hat{\theta}$, with the phase $\hat{\theta}(t) = \hat{\theta}_0 + \hat{\omega}t$ and the frequency $\hat{\omega} = 2\pi \hat{S}t$. The hat marks estimated quantities.

The parameters \hat{c}_0 and \hat{c}_1 are assumed to be slowly varying (nominally, constant) and $\hat{\theta}$ is assumed to grow linearly; their instantaneous values are estimated in real time by a dynamic observer, realized by an extended Kalman filter (EKF), which is described in Appendix B. Based on the estimated phase $\hat{\theta}$, a harmonic actuation signal $g(t) = A \sin(\hat{\theta} + \Delta\phi)$ is calculated and applied to the upper actuator slot only. The term $\Delta\phi = 180^\circ$ represents the desired angle between actuation and pressure readings as discussed in §4. The amplitude A corresponds to a momentum coefficient of $c_\mu = 7.5 \times 10^{-3}$. Since we only use a single actuator, the effective impulse contribution is only half that amount ($c_\mu^{eff} = 3.8 \times 10^{-3}$).

5.2.2. Experimental results of phase control

Our proposed phase controller is tested in our experimental rig at Reynolds number 46 000. Control is applied at $t=0$ and decreases the drag at the same rate as open-loop forcing or slope-seeking feedback with optimal actuation parameters (figure 15). Time series of the sensed and estimated pressure oscillations at the lower edge are in good agreement, indicating a proper estimation of the amplitude \hat{c} and phase $\hat{\theta}$ (figure 15a). The estimated frequency of the leading harmonic displayed in figure 15(b) is close to the natural instability frequency of $St \approx 0.23$, when actuation is off, and decreases to $St \approx 0.15$ when control is applied. Based on the phase estimation an almost harmonic actuation signal for the upper actuator is calculated (figure 15c). The normalized drag coefficient plotted in figure 15(d) decreases by at least 15% after ten vortex shedding periods. Comparing the effective impulse coefficient $c_\mu^{eff} = 3.8 \times 10^{-3}$ used here, with the results of slope-seeking feedback at $Re_H = 46\,000$ ($c_\mu \approx 6.7 \times 10^{-3}$, see figure 12b), we only need 56% of the actuation energy.

Hot-wire measurements in the controlled flow, as described in §3.3 for the natural and open-loop forced flow to corroborate the predominantly two-dimensional character of the coherent structures, are presented in figure 16(a,b). The coherent structures remain two-dimensional under feedback control as well.

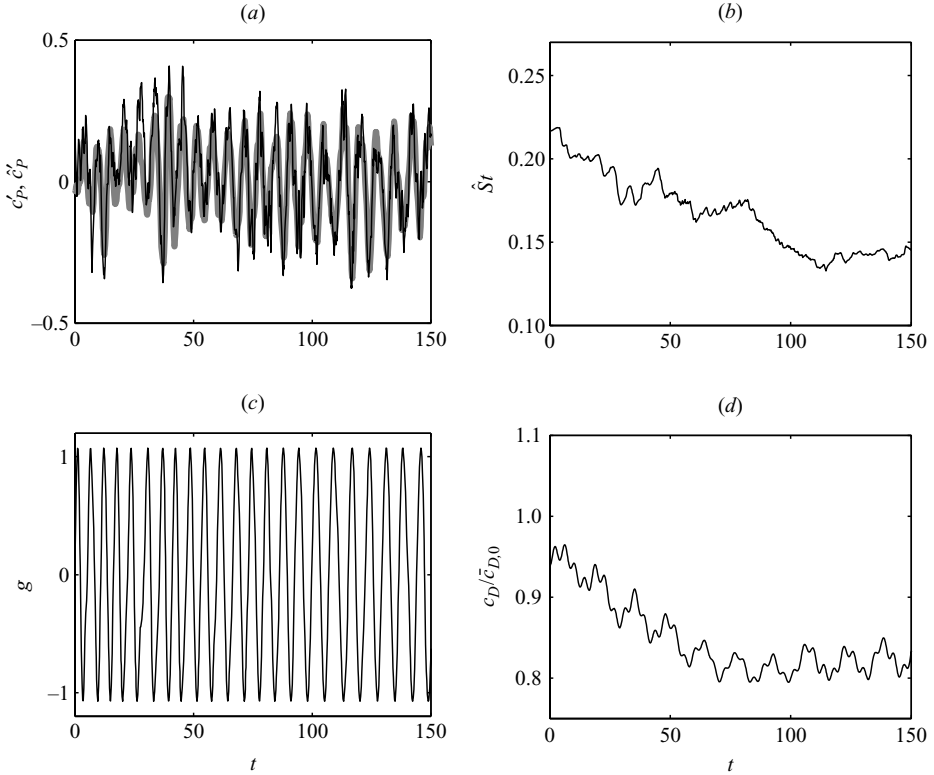


FIGURE 15. Phase control in experiment at $Re_H = 46000$ (see figure 14). Control starts at $t = 0$. In (a), pressure readings at the lower edge (sensed —, estimated —) are displayed. The estimated oscillation frequency and applied actuation signal are plotted in (b) and (c). The success is demonstrated by the decrease of the normalized drag coefficient in (d).

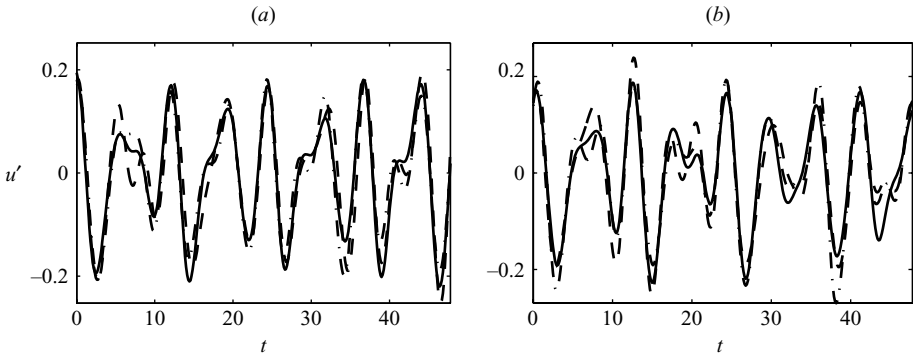


FIGURE 16. The same as figure 6, but for the phase controller in experiment at $Re_H = 46000$.

Robustness to changing operating conditions of the phase controller is demonstrated by a sweep of the Reynolds number from 23 000 to 70 000 (figure 17a). As indicated by figure 17(b), the average drag is reduced by 15% compared to the natural flow, throughout the experiment.

The importance of adding $\Delta\phi = 180^\circ$ to the estimated phase before calculating the actuation signal is elucidated in figure 18. Control is applied to the steady-state base

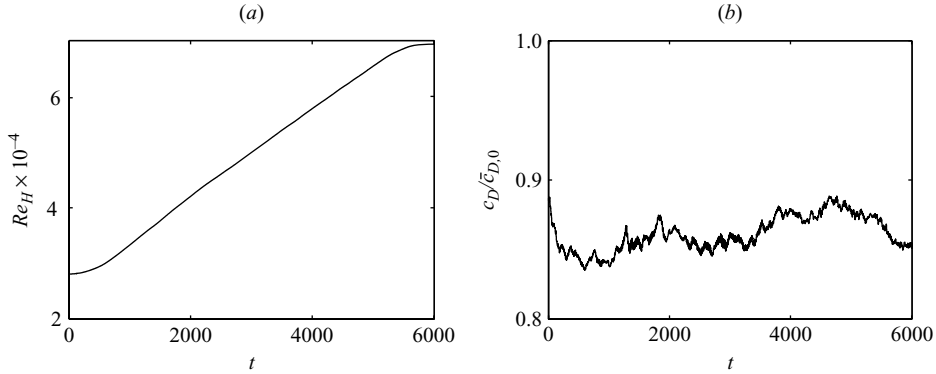


FIGURE 17. Phase control in experiment for changing operating conditions. While the Reynolds number increases from 29 000 to 70 000 (a), the average drag remains almost constant at 15% below the baseline (b). Time is normalized by the oncoming velocity associated with $Re_H = 46\,000$.

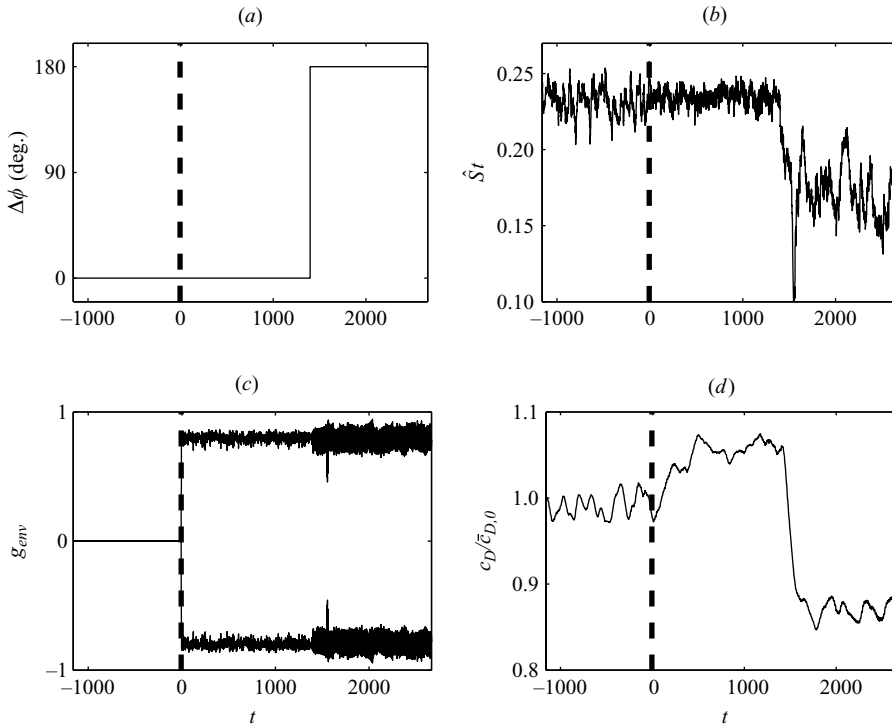


FIGURE 18. Phase control in experiment at $Re_H = 46\,000$ with two modes: control starts at $t=0$ in mode (1) with $\Delta\phi = 0^\circ$, and switches to mode (2) at $t=1400$ when $\Delta\phi$ jumps to 180° (a). The estimated oscillation frequency $\hat{S}t$ and the envelope of the applied actuation signal g_{env} are plotted in (b) and (c), respectively. Drag increases while applying $\Delta\phi = 0^\circ$, thus amplifying the natural alternating vortex shedding, and decreases for $\Delta\phi = 180^\circ$, where symmetrical vortex shedding from both shear layers is enforced (d).

flow at $t=0$ with $\Delta\phi = 0^\circ$ (figure 18a). In this mode, the alternating character of vortex shedding is enhanced, as can be seen by the increase of drag (figure 18d) and the accentuation of the natural instability frequency (figure 18b). At $t=1400$, the

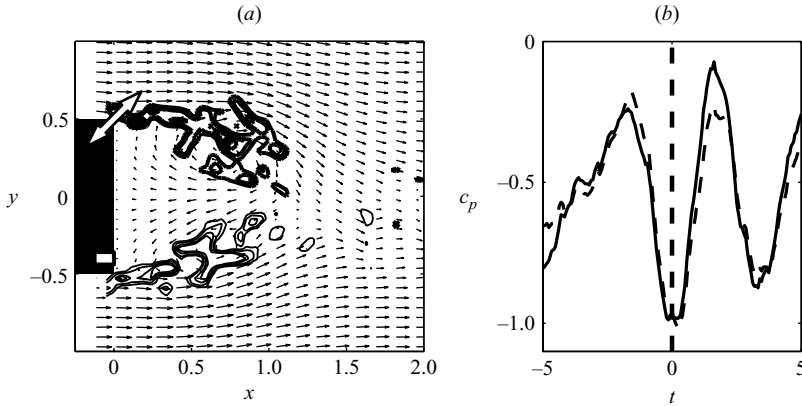


FIGURE 19. The same as figure 3(a,b), but for the implemented phase controller in experiment. The sensor at the lower edge is marked by a rectangle at the stern of the body. Actuation is applied at the upper edge only.

phase offset is increased to $\Delta\phi = 180^\circ$. Drag and estimated frequency take the values described before.

In figure 19, the instantaneous vorticity field obtained from PIV at $Re_H = 23\,000$ is displayed. The coherent structures resemble those that appear in the open-loop forced flow (figure 5a). The controller tunes itself to an average excitation frequency of $St_A \approx 0.15$. We emphasize, that this frequency is not explicitly selected, but is a result of linking the upper to the lower shear layer evolution.

The controller is able to mimic the effect of two actuators while in fact using only a single actuator. This ‘redundancy’ has two beneficial consequences. Firstly, energy can be saved, since only one actuator is required. Thus, regarding the power requirement of a single actuator and the power saved due to drag reduction, a gain of 4.5 is found. A second benefit—and this is even more important—is a proof of our physical understanding of the flow. Our control idea, to directly decouple wake and shear layer processes by synchronization, is the key to explaining and improving the mechanics of drag reduction in wake flows.

6. Conclusions and outlook

In this study, we have proposed open- and closed-loop control strategies that achieve up to 40% base pressure increase associated with a 15% drag reduction for the D-shaped body. The net energy balance is positive: the invested actuation power is returned by more than four times via the associated reduction of towing power. In the current experimental setup, actuation was only applied to half the span width of the body. Applying actuation to only a quarter of the span width almost halves the achieved drag reduction. Extrapolating the almost linear relation between drag reduction and spanwise actuator extent, we expect an increase of the drag reduction from 15% to up to 30% when extending actuation to the full span. Additionally, the return per actuation power investment could be increased by more efficient actuators.

The key enabler for energy-efficient control design was the physical understanding obtained from a reduced-order vortex model. This model resolves the coherent flow structures and the effects of actuation. The natural flow is characterized by a short dead water region and alternating eddies in the vicinity of the base. Both are

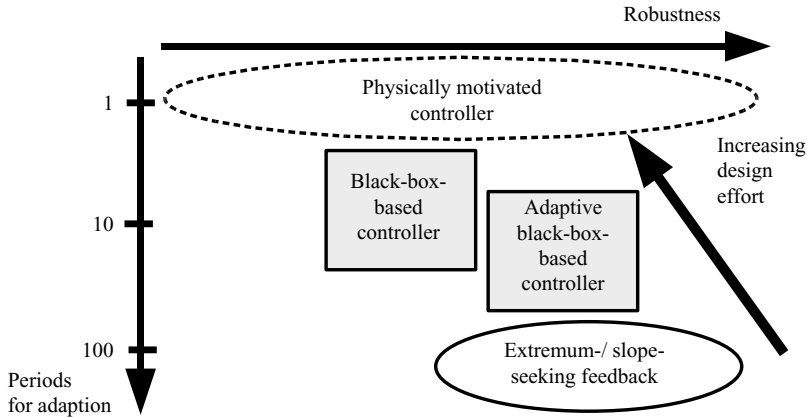


FIGURE 20. Time scales, robustness and required modelling effort of different controllers.

responsible for a low base pressure and thus for a high drag. The proposed controllers enforce a decoupling of the vortex formation in the shear layers and the wake by synchronizing the roll-up of upper and lower shear layers. This delays the appearance of asymmetries and thus suppresses the effects of the wake instability. The dead water region is enlarged and the base pressure increases.

Evidently, our control approach is based on a choice of actuators, sensors and a control law tailored to a model-based control mechanism. The question arises whether the control law can be improved and if targeting other physical control mechanisms might be more efficient. In principle, our control idea can be realized by open-loop control. However, actuation frequency and amplitude have to be selected carefully depending on the Reynolds number. Otherwise, actuation energy is wasted. In the worst case, actuation can even increase the drag by amplifying the wake instability. Nonetheless, industrial application of open-loop control for drag reduction of trucks† and compact‡ cars, by blowing at the trailing edges, is imminent.

Closed-loop schemes can enhance efficiency of active control in a wide range of operating conditions. The benefits and drawbacks of different closed-loop controllers are outlined in figure 20.

Controllers based on black-box models are useful for stabilizing a working point. In this study, we are interested in minimizing the drag, rather than stabilizing a certain condition. Therefore, black-box control was not investigated. Instead, slope-seeking feedback is utilized for an automatic adaptation of the optimal actuation amplitude under changing Reynolds numbers. The controller operates on a time scale that is two orders of magnitude larger than the vortex shedding period. Robustness and ease of implementation in experiment make this approach convenient for automatic identification of good actuation parameters. The most efficient control is realized by a physically motivated phase controller which explicitly synchronizes upper and lower shear layer evolution by design. This controller is tailored to the key physical processes of the system, which are obtained from a coherent structure model. This has two advantages. Firstly, the control goal can be achieved with a lower level of actuation energy. Secondly, the adaptation of the controller to disturbances and changing operation conditions is fast, since it operates on the time

† e.g. Volvo, Great Dane Trailers, Georgia Tech.

‡ e.g. Renault Altica.

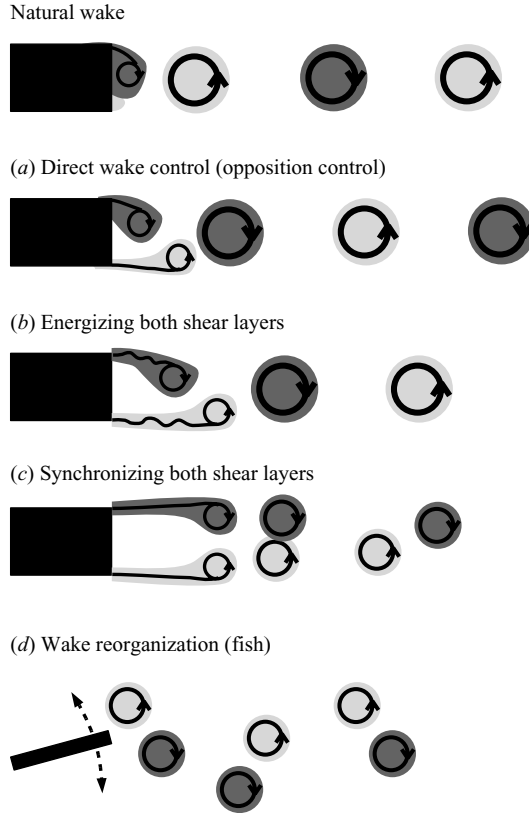


FIGURE 21. Drag reduction by different active means of wake manipulation. For details, see text.

scale of the physical processes. Often, a physically motivated controller exhibits less robustness compared to gradient-based controllers, since it is bound to the range of validity of the nonlinear reduced-order model. However, the vortex shedding process investigated in this study is stable for arbitrary Reynolds numbers, which ties robustness to the ability to properly identify the shedding phase.

Our drag reduction strategy relates to other physical mechanisms that allow wake control, as indicated in figure 21. These other approaches include direct methods of opposition control and indirect methods to energize the shear layers.

Numerical and experimental investigations of opposition control were conducted by Siegel *et al.* (2003) and Gerhard *et al.* (2003) for the cylinder flow based on reduced-order POD models. Actuation is affected by transversal oscillations of the cylinder or an oscillatory volume force applied downstream of the cylinder, respectively. Both methods achieve an elongated recirculation bubble by a direct opposition control (figure 21a) of the wake structures. Applicability is restricted to the laminar Reynolds numbers regime, as turbulent flows tend to elude suppression strategies by forming new structures.

Wake control by energizing the shear layers (figure 21b) was investigated by several authors with different control methods. Park *et al.* (2006) propose passive vortex disruptors (tabs), which enlarge the dead water region by mitigating the development of large vortical structures. The study includes experiments and large-eddy simulations in a range of Reynolds numbers from 20 000 to 80 000 and 320 to 4200, respectively.

The base pressure increases by 30% for an optimized tab configuration. A similar but active controller was proposed by Kim *et al.* (2004). Protas & Wesfreid (2002) numerically studied the effect of open-loop control on the formation of the wake flow behind a cylinder at a Reynolds number based on the diameter of 150. They obtained results similar to those presented in our study. A significant drag reduction is related to an elongation of the recirculation bubble by supporting an unstable symmetric state. Control is applied by cylinder rotations at various frequencies, which turned out to be energetically inefficient at low Reynolds numbers. Wu *et al.* (2007) completely suppressed the von Kármán vortex street of a circular cylinder. In their numerical investigation at Reynolds numbers up to 5000 a drag reduction of 85% was achieved by generating travelling waves on the flexible surface of the body. The invested power for actuating the surface is found to be 94% of the power saving. Extremum-seeking feedback control was applied by Beaudoin *et al.* (2006) to a bluff body configuration that is similar to a backward-facing step. Actuation is implemented by a rotating cylinder at the trailing edge. The rotation frequency is adaptively controlled in order to minimize the drag (up to 5%) with a given power requirement.

The phase controller proposed in this study marks a change of paradigm. The two-dimensional phase control strategies investigated by Siegel *et al.* (2003) and Gerhard *et al.* (2003) aim at a suppression of the wake structures, by generating anti-cyclic control forces. As mentioned before, these methods are restricted to a laminar regime. The proposed strategy promotes symmetrical shear layer structures without significantly energizing their fluctuation level. Thus, the formation of the vortex street is delayed at low-actuation amplitudes (figure 21c). Furthermore, our strategy seems to be applicable in a turbulent regime.

The very mechanism of intervening in the coupling between the shear layers and the vortex formation can be envisioned to be applicable to three-dimensional flow configurations, e.g. for flows behind spheres. A rigorous comparison is still needed to verify this understanding. It should be noted that nature provides its own solution to reducing wake-induced drag (figure 21d): the strokes of a fishtail create a propulsive jet flow, by inverting the vortical structure in the wake (Ahlborn 2004).

The authors emphasize the superiority of feedback control in contrast to open-loop control. In steady low-turbulent wind tunnel experiments open-loop actuation may be optimized to a level which is comparable to closed-loop control. In real world applications flow control has to cope with varying oncoming velocities, high turbulence levels and other perturbations. Hence, by utilizing feedback design, the benefits of active flow control can be fully exploited. In future work, the authors will pursue the direct usage of reduced-order vortex and Galerkin models as plants for control and observer design, targeting the industrial application of closed-loop flow control.

The work was funded by the Deutsche Forschungsgemeinschaft (DFG) under grants NO 258/1-1 and NO 258/2-3, by a CNRS invited researcher grant, by the US National Science Foundation (NSF) under grants 0524070 and 0410246, and by the US Air Force Office of Scientific Research (AFOSR) under grants FA95500510399 and FA95500610373. The authors acknowledge funding and excellent working conditions of the Collaborative Research Centre (Sfb 557) ‘Control of Complex Turbulent Shear Flows’, supported by the DFG and hosted at the Berlin Institute of Technology. Stimulating discussions with Katarina Aleksic, Laurent Cordier, Hans-Christian Hege, Oliver Lehmann, Mark Luchtenburg, Eckart Meiburg, Marek Morzyński, Michael Schlegel, Jon Scouten, Avi Seifert, Stefan Siegel, Tino Weinkauff, and Jose-Eduardo

Wesfreid are acknowledged. We are grateful for outstanding hardware and software support by Joachim Kraatz, Frank Kunze, Ingolf Richter, Lars Oergel and Martin Franke and excellent administration of our Sfb 557 by Steffi Stehr.

Appendix A. Vortex model

In this section, the building blocks of the vortex model are outlined. We recapitulate the kinematics of the model from (2.1) for convenience, and decompose the stationary potential Φ_s from the unsteady actuation potential Φ_a :

$$\mathbf{u}(\mathbf{x}, t) = \nabla\Phi_s(\mathbf{x}) + \nabla\Phi_a(\mathbf{x}, t) + \sum_{i=1}^N \Gamma_i \mathbf{u}^\omega(\mathbf{x}, \mathbf{x}_i). \quad (\text{A } 1)$$

A.1. Conformal mapping

Following Clements (1973), Evans & Bloor (1977), Cortelezzi (1996) and Coller *et al.* (2000), the no-penetration condition is enforced by employing a conformal mapping. This procedure is computationally cheaper and more accurate for low-order vortex models compared with a computational panel approach (see e.g. Fletcher 1988). The conformal map bijectively transforms the computational domain – the upper half-plane $\zeta = \xi + i\eta$ with $\xi \in \mathbb{R}$ and $\eta \in \mathbb{R}^+$ – into the physical domain. In the computational domain, the no-penetration condition with discrete vortices is satisfied by introducing image vortices with the abscissae as the axis of reflection.

The conformal mapping from the computational domain, $\zeta = \xi + i\eta$, into the physical domain, $z = x + iy$, is obtained by integration of the following Schwarz–Christoffel transformation:

$$\frac{dz}{d\zeta} = C_1 \frac{\sqrt{\zeta^2 - 1}}{\zeta^2 - a^2}, \quad \text{where } C_1, a \in \mathbb{R}. \quad (\text{A } 2)$$

The map $z(\zeta)$ is expressed by

$$\begin{aligned} z(\zeta) = & C_2 + C_1 \frac{1}{2a} \left(2a \log(\zeta + \sqrt{\zeta^2 - 1}) \right. \\ & - \sqrt{a^2 - 1} \log \left(\frac{1 - a\zeta - \sqrt{a^2 - 1}\sqrt{\zeta^2 - 1}}{-\zeta + a} \right) \\ & \left. + \sqrt{a^2 - 1} \log \left(\frac{-1 - a\zeta + \sqrt{a^2 - 1}\sqrt{\zeta^2 - 1}}{\zeta + a} \right) \right), \quad C_2 \in \mathbb{C}. \quad (\text{A } 3) \end{aligned}$$

The constants $a/\sqrt{a^2 - 1} = h/(h - H)$, $C_1 = h/\pi$ and $C_2 = -7i$ are obtained from the equation of continuity and from geometrical considerations. The imaginary unit is denoted by i . The inverse mapping $\zeta(z)$ is calculated numerically with the Newton–Raphson method. No analytical solution has been found.

A.2. Potential flow

Vortex models yield potential flow solutions of the Navier–Stokes equation with singularities at the vortex loci. The conformal mapping is used to satisfy the no-penetration condition at the walls in an efficient manner. The potential flow solution is generated by a pair of point sources at $\zeta_i = \pm a$, which is mapped to $x \rightarrow -\infty$. The complex source potential is transformed to the physical domain by applying the

chain rule of differentiation:

$$\begin{aligned}\frac{dW_s^\zeta}{d\zeta} &= \sum_{n=1}^2 \frac{Q_n}{2\pi} \frac{1}{\zeta - \zeta_n}, \\ \frac{dW_s^z}{dz} &= \frac{dW_s^\zeta}{d\zeta} \frac{d\zeta}{dz} =: w_s^z(z), \\ \nabla\Phi_s(\mathbf{x}) &= \begin{pmatrix} \text{Re}\{w_s^z(z)\} \\ -\text{Im}\{w_s^z(z)\} \end{pmatrix}.\end{aligned}\quad (\text{A } 4)$$

The source strength $Q_n = 2h/(h - H)$ corresponds to the flow rate in each cross-section of the physical domain. The velocity field generated by both sources in the physical domain describes a potential flow around the aft section of the D-shaped body without separation. The abscissa of the ζ -plane represents wall streamlines in the physical domain.

A.3. Actuation

The actuation is modelled by two harmonic oscillating sources near the trailing edges of the body, – following the authors' work for the backward-facing step configuration in Pastoor *et al.* (2003). Thus, for the actuated flow, a time-dependent potential is added to the potential flow. The corresponding velocity field reads

$$\nabla\Phi_a(\mathbf{x}, t) = \begin{pmatrix} \text{Re}\{w_a^z(z, t)\} \\ -\text{Im}\{w_a^z(z, t)\} \end{pmatrix}, \quad (\text{A } 5)$$

where

$$\begin{aligned}\frac{dW_a^z(t)}{dz} &= \frac{dW_a^\zeta}{d\zeta} \frac{d\zeta}{dz} =: w_a^z(z, t), \\ \frac{dW_a^\zeta(t)}{d\zeta} &= \sum_{n=1}^2 \frac{Q_n(t)}{2\pi} \frac{1}{\zeta - \zeta_n}.\end{aligned}$$

This field fulfils the boundary conditions, as long as the sources are placed on the contour of the body. The position ζ_n of the actuators is adjusted to blow with an angle of attack of 45° at the point of insertion of vortices (see below). The strength $Q_n(t)$ depends on the selected actuation. The instantaneous mass flux into the upper half-plane is chosen to be similar to the corresponding quantity of the actuators in experiment.

A.4. Vortex elements

The no-penetration condition for a potential flow superimposed onto a vortex flow is fulfilled with a virtual vortex with mirrored coordinates and opposite circulation. Similarly, an ensemble of vortices is supplemented by their image vortices. The N vortices at the time t in the physical domain induce the velocity

$$\mathbf{u}^\omega(\mathbf{x}, t) = \begin{pmatrix} \text{Re}\{w_v^z(z, t)\} \\ -\text{Im}\{w_v^z(z, t)\} \end{pmatrix}, \quad (\text{A } 6)$$

where

$$\begin{aligned}\frac{dW_v^z(t)}{dz} &= \frac{dW_v^\zeta}{d\zeta} \frac{d\zeta}{dz} =: w_v^z(z, t), \\ \frac{dW_v^\zeta(t)}{d\zeta} &= -i \sum_{n=1}^N \frac{\Gamma_n}{2\pi} \frac{1}{\zeta - \zeta_n(t)} + i \sum_{n=1}^N \frac{\Gamma_n}{2\pi} \frac{1}{\zeta - \bar{\zeta}_n(t)}.\end{aligned}$$

The coordinate ζ_n denotes the current position of the n th vortex and Γ_n its circulation. The overbar indicates the complex conjugate of a complex number. The circulation Γ_n of each vortex is preserved according to Kelvin's law. When the velocity is prescribed at the centre of the vortex element, the velocity calculation is modified according to Routh's theorem (Milne-Thomson 1968). In this case, the induced complex velocity at z_n reads

$$w_v^z(z_n, t) = \left(-i \sum_{\substack{j=1 \\ j \neq n}}^N \frac{\Gamma_j}{2\pi} \frac{1}{\zeta_n - \zeta_j(t)} + i \sum_{j=1}^N \frac{\Gamma_j}{2\pi} \frac{1}{\zeta_n - \bar{\zeta}_j(t)} \right) \frac{d\zeta}{dz} \Big|_{z_n} - i \frac{\Gamma_n}{2\pi} \frac{d^2\zeta/dz^2}{2 d\zeta/dz} \Big|_{z_n}.$$

Up to now, a point vortex discretization has been assumed in agreement with potential flow theory. The discontinuity in the vortex field is regularized in a more refined model by Hamel and Oseen. Their solution for the azimuthal velocity u_φ as a function of the distance r between vortex and sample point smoothly connects a Rankine vortex core at $r \rightarrow 0$ with the potential vortex at $r \rightarrow \infty$,

$$u_\varphi(r) = \frac{\Gamma_0}{2\pi r} (1 - e^{-r^2/R^2}) \quad (\text{A } 7)$$

where R denotes the core radius of the vortex. The initial core radius at the trailing edges is chosen to be similar to the boundary layer thickness. A linear temporal growth of the core diameter is implemented to account for turbulent diffusion of vorticity.

A.5. Vorticity production

Experiments and simulations indicate straight shear layers emerging from the upper and lower edges of the body in the direction of the oncoming flow. Giesing (1969) proposes a *generalized Kutta condition* for the idealized infinitely thin shear layer in inviscid flow. According to this condition, the shear layer is aligned with the oncoming flow. The circulation contribution $d\Gamma$ of a small shear layer segment of the length dx is

$$d\Gamma = (U_{lower} - U_{upper}) dx, \quad (\text{A } 8)$$

where U_{upper} and U_{lower} are the velocities above and below the shear layer, respectively. This criterion is in good agreement with experimental and numerical investigations of the flow around a D-shaped body.

In our vortex model, Giesing's solution is discretized by inserting vortices each time step Δt with a circulation $|\Gamma| = U_1^2 \Delta t / 2$ at $x = U_1 \Delta t / 4$ and $y = \pm 0.5$ (Clements 1973). The circulation of vortices is negative at the upper edge and positive at the lower edge. The velocity U_1 is computed at $y = \pm 0.7$. To avoid numerical problems with the singularities of the Schwarz–Christoffel transformation at both edges, vortices are lead a short distance away from the singularity ($x < 0.05$).

A.6. Vortex merging

A discretization parameter of our model is the number of vortices consistent with the desired low-dimensionality. The perpetual creation of new vortices increases the order of our model. This order can be reduced by merging two vortices when their distance is below a critical value. The result of a merging process is one vortex with the combined circulation located at the barycentre of both predecessors. A reasonable compromise between accuracy and dimensionality is obtained by a merging distance which increases linearly from $R=0.05$ at $x=0$ to $R=0.5$ at $x \leq 10$.

Appendix B. Extended Kalman Filter

An extended Kalman filter (EKF) is an established and efficient method to estimate the state of a dynamical system from a series of incomplete or noisy measurements. A good source is Gelb (1986) and a description of the method used here can be found in Tadmor (2004). For completeness, this section begins with a brief review of the EKF framework, followed by the specifics of the implementation used in this article.

A dynamical system can be described by

$$\dot{\mathbf{a}} = \mathbf{f}(\mathbf{a}, \mathbf{g}, t) + \dot{\mathbf{w}} \quad (\text{B } 1)$$

where \mathbf{a} is the true state of the system, \mathbf{g} represents control variables and $\dot{\mathbf{w}}$ is a zero-mean white noise process with spectral density Q (obtained from a Wiener process \mathbf{w}). A measurement of the true state at discrete times is made according to

$$s_k = \mathbf{h}(\mathbf{a}_k, \mathbf{g}_k, t_k) + \mathbf{v}_k, \quad (\text{B } 2)$$

where \mathbf{v}_k is observation noise with covariance R_k .

The state of the Kalman filter is represented by two variables, namely the estimated state $\hat{\mathbf{a}}$ and the error covariance matrix P , which is a measure of the estimated accuracy of the state estimate. The Kalman filter has the following two distinct phases.

Prediction (time update). In this phase no measurement is available. The estimated state from the previous time t_{k-1} is used to produce an estimation of the current state at time t_k , here by a simple Euler step:

$$\hat{\mathbf{a}}_k = \hat{\mathbf{a}}_{k-1} + \mathbf{f}(\hat{\mathbf{a}}_{k-1}, \mathbf{g}_{k-1}, t_{k-1}) \Delta t. \quad (\text{B } 3)$$

The covariance of the estimation error changes according to

$$P_k = P_{k-1} + (F_{k-1} P_{k-1} + P_{k-1} F_{k-1}^T + Q) \Delta t. \quad (\text{B } 4)$$

Here, F is the Jacobian of the dynamical system evaluated with the current state estimate

$$F_k = \left. \frac{\partial \mathbf{f}}{\partial \mathbf{a}} \right|_{\hat{\mathbf{a}}_k, \mathbf{g}_k}. \quad (\text{B } 5)$$

Update (measurement update). In this phase, current measurement information is used to refine the prediction. In the following, all states are marked by superscript $(-)$ before and by $(+)$ after the measurement update. The estimated state is corrected based on the innovation or measurement residual

$$\Delta \hat{\mathbf{s}}_k = s_k - \mathbf{h}(\hat{\mathbf{a}}_k^-, \mathbf{g}_k, t_k) \quad (\text{B } 6)$$

and the optimal Kalman gain

$$K_k = P_k^- H_k^T (H_k P_k^- H_k^T + R_k)^{-1}, \quad (\text{B } 7)$$

where H_k is the Jacobian of the output equation evaluated with the predicted state

$$H_k = \left. \frac{\partial \mathbf{h}}{\partial \mathbf{a}} \right|_{\hat{\mathbf{a}}_k^-, g_k}. \quad (\text{B } 8)$$

The updated state estimate is

$$\hat{\mathbf{a}}_k^+ = \hat{\mathbf{a}}_k^- + K_k \Delta \hat{\mathbf{s}}_k, \quad (\text{B } 9)$$

while the updated estimate of the covariance matrix is

$$P_k^+ = (I - K_k H_k) P_k^-. \quad (\text{B } 10)$$

Q and R_k have an intuitively clear meaning for a one-dimensional system. When R_k is large, the filter does not trust in the measurement. The computed Kalman gain (B 7) is small and thus the filter prefers the state estimate already in the model (B 9). Vanishing R_k indicates an ideal sensor and the Kalman gain is $1/H_k$. After the measurement update the covariance of the estimation error is exactly zero (B 10). When Q is large, the filter expects a lot of process noise. The covariance of the estimation error grows rapidly with each time update (B 4). In the measurement update, the filter prefers information from the measurement over the predicted state.

In our application, pressure fluctuations at the base of the D-shaped body are approximated by a sine function $c_p(t) = s = c_0 + c_1 \sin \theta$. We assume a dynamical model with the four states frequency ω , amplitude c_1 , phase θ and offset c_0 , which are combined in a state-space vector

$$\mathbf{a} = \begin{pmatrix} \omega \\ \theta \\ c_1 \\ c_0 \end{pmatrix}.$$

Pressure fluctuations are then described by the output equation

$$s_k = h(\mathbf{a}_k) = a_{2,k} \sin a_{3,k} + a_{4,k}.$$

A simple stochastic state-space model for the temporal evolution is provided by

$$\mathbf{a}_k = \underbrace{\begin{bmatrix} 1 & 0 & 0 & 0 \\ \Delta t & 0 & 1 & 0 \\ 0 & 1 & 0 & 0 \\ 0 & 0 & 0 & 1 \end{bmatrix}}_F \mathbf{a}_{k-1} + \mathbf{w}_{k-1}.$$

This means that frequency, amplitude and offset are considered nominally constant, while the phase grows with time according to the current frequency. A fair approximation of Q is obtained when the estimated variances of the states divided by T are placed along the diagonal. Here, T is the expected time scale on which the variances of the states appear. The same procedure is applied to the matrix R_k with the variance of the measurement noise over T . Thus, covariance matrices of process and measurement noise are supposed to be

$$Q = \begin{bmatrix} 200 & 0 & 0 & 0 \\ 0 & 0 & 0.01 & 0 \\ 0 & 1 & 0 & 0 \\ 0 & 0 & 0 & 1 \end{bmatrix} \times 10^{-2} \quad \text{and} \quad R_k = 5 \times 10^{-2}.$$

Re_H	Actuation	Position y	$\angle u_c u_{c-2}$ [deg.]	$\angle u_c u_{c-1}$ [deg.]	$\angle u_c u_{c+1}$ [deg.]	$\angle u_c u_{c+2}$ [deg.]
23 000	natural flow	+0.7	-0.5	0.1	0.3	-1.3
		-0.7	2.1	1.5	2.1	2.0
	open-loop $St_A = 0.15, c_\mu = 0.015$	+0.7	-0.7	0.0	0.6	2.5
		-0.7	-0.5	1.1	-0.2	0.5
phase control $c_\mu = 0.009$	+0.7	-0.9	0.7	-0.1	0.2	
	-0.7	0.2	-0.7	-2.6	0.3	
35 000	natural flow	+0.7	-0.3	0.0	0.0	0.5
		-0.7	1.3	1.6	1.3	1.1
	open-loop $St_A = 0.15, c_\mu = 0.013$	+0.7	0.8	-0.2	-0.2	2.8
		-0.7	2.0	-0.1	0.0	-0.6
phase control $c_\mu = 0.008$	+0.7	-2.0	-0.1	-0.1	-0.9	
	-0.7	1.3	0.4	0.4	0.0	
46 000	natural flow	+0.7	0.3	0.6	-0.4	0.1
		-0.7	0.5	-0.3	0.2	1.2
	open-loop $St_A = 0.15, c_\mu = 0.012$	+0.7	-3.9	-0.5	-0.1	-5.7
		-0.7	-3.5	0.4	-0.3	-5.7
phase control $c_\mu = 0.007$	+0.7	0.0	0.8	0.7	-0.4	
	-0.7	0.0	-0.8	-0.5	-0.5	
58 000	natural flow	+0.7	0.3	0.6	0.4	-0.7
		-0.7	0.4	-0.5	-1.0	0.3
	open-loop $St_A = 0.15, c_\mu = 0.010$	+0.7	6.9	0.0	0.4	2.3
		-0.7	-2.7	-0.2	0.0	-4.9
phase control $c_\mu = 0.007$	+0.7	-0.9	0.3	-0.4	-1.0	
	-0.7	0.5	2.2	0.5	1.5	
70 000	natural flow	+0.7	0.0	1.8	0.2	-0.1
		-0.7	-0.2	0.6	0.4	-1.0
	open-loop $St_A = 0.15, c_\mu = 0.009$	+0.7	-7.3	-0.1	-0.2	-14.8
		-0.7	3.8	-0.2	-0.2	-7.4
phase control $c_\mu = 0.006$	+0.7	0.9	0.7	-2.3	0.7	
	-0.7	0.4	-0.4	0.3	-0.9	

TABLE 3. Spanwise phase delay of dominant velocity fluctuations. Hot-wire probes are mounted in spanwise arrays at $(x, y) = (1, \pm 0.7)$. Phase angles are computed between fluctuations at $z = 0$ (u_c) and $z = \pm 1.15$ ($u_{c\pm 1}$), and $z = \pm 1.74$ ($u_{c\pm 2}$), respectively, using the Fourier decomposition for the corresponding dominant frequency.

Initial filter states $\hat{\mathbf{a}}_0$ and P_0 are set to

$$\hat{\mathbf{a}}_0 = \begin{bmatrix} 2\pi \times 0.23 \\ 0.1 \\ 0.0 \\ -0.5 \end{bmatrix} \quad \text{and} \quad P_0 = \begin{bmatrix} 40 & 0 & 0 & 0 \\ 0 & 0 & 2 & 0 \\ 0 & 1 & 0 & 0 \\ 0 & 0 & 0 & 1 \end{bmatrix} \times 10^{-2}.$$

Appendix C. Additional data

In table 3 the phase differences as described in §3.3 are summarized for all investigated Reynolds numbers.

REFERENCES

- AHLBORN, B. K. 2004 *Zoological Physics*. Springer.
- ARIYUR, K. & KRSTIĆ, M. 2003 *Real-Time Optimization by Extremum-Seeking Control*. John Wiley & Sons.
- BEALE, J. T. & MAJDA, A. 1982 Vortex methods I: Convergence in three dimensions. *Math. Comput.* **39**, 1–27.
- BEARMAN, P. W. 1965 Investigation of the flow behind a two-dimensional model with a blunt trailing edge and fitted with splitter plates. *J. Fluid Mech.* **21**, 241–255.
- BEARMAN, P. W. 1967 The effect of base bleed on the flow behind a two-dimensional model with a blunt trailing edge. *Aeronaut. Q.* **18**, 207–224.
- BEAUDOIN, J. F., CADOT, O., AIDER, J.-L., & WESFREID, J.-E. 2006 Drag reduction of a bluff body using adaptive control methods. *Phys. Fluids* **18**, 08510.
- BECKER, R., GARWON, M., GUTKNECHT, C., BÄRWOLFF, G. & KING, R. 2005 Robust control of separated shear flows in simulation and experiment. *J. Process Control* **15**, 691–700.
- BECKER, R., KING, R., PETZ, R. & NITSCHKE, W. 2007 Adaptive closed-loop separation control on a high-lift configuration using extremum seeking. *AIAA J.* **45**, 1382–1392.
- BERGMANN, M., CORDIER, L. & BRANCHER, J.-P. 2005 Optimal rotary control of the cylinder wake using proper orthogonal decomposition reduced order model. *Phys. Fluids* **17**, 1–21.
- BIRKHOFF, G. 1962 Helmholtz and Taylor instability. In *Proc. Symp. Appl. Maths XII*, pp. 55–76. AMS.
- CATTAFFESTA, L., WILLIAMS, D. R., ROWLEY, C. W. & ALVI, F. 2003 Review of active control of flow-induced cavity resonance. *AIAA Paper* 2003-3567.
- CLEMENTS, R. R. 1973 An inviscid model of two-dimensional vortex shedding. *J. Fluid Mech.* **57**, 321–336.
- COLLER, B. D., NOACK, B. R., NARAYANAN, S., BANASZUK, A. & Khibnik, A. I. 2000 Reduced-basis model for active separation control in a planar diffuser flow. *AIAA Paper* 2000-2563.
- COLLIS, S. S., JOSLIN, R. D., SEIFERT, A. & THEOFILIS, V. 2004 Issues in active flow control: theory, control, simulation, and experiment. *Prog. Aerospace Sci.* **40**, 237–289.
- COOPER, K. R. 1985 The effect of front-edge rounding and rear edge shaping on the aerodynamic drag of bluff vehicles in proximity. *SAE Paper* 850288.
- CORDIER, L. & BERGMANN, M. 2003 *Proper Orthogonal Decomposition: An Overview*. VKI Lecture Series 2003–04. Von Kármán Institut for Fluid Dynamics.
- CORTELEZZI, L. 1996 Nonlinear feedback control of the wake past a plate with a suction point on the downstream wall. *J. Fluid Mech.* **327**, 303–324.
- COTTET, G. H. & KOUMOUTSAKOS, P. 2000 *Vortex Methods – Theory and Practice*. Cambridge University Press.
- DETEMPLE-LAAKE, E. & ECKELMANN, H. 1989 Phenomenology of Kármán vortex streets in oscillatory flow. *Exps. Fluids* **7**, 217–227.
- EVANS, R. A. & BLOOR, M. I. G. 1977 The starting mechanism of wave-induced flow through a sharp-edged orifice. *J. Fluid Mech.* **82**, 115–128.
- FIEDLER, H.-E. & FERNHOLZ, H. H. 1990 On management and control of turbulent shear flows. *Prog. Aeronaut. Sci.* **27**, 305–387.
- FLETCHER, C. A. J. 1988 *Computational Techniques for Fluid Dynamics; Volume II: Specific Techniques for Different Flow Categories*. Springer.
- GAD-EL-HAK, M., POLLARD, A. & BONNET, J.-P. 1998 *Flow Control - Fundamentals and Practices*. Springer.
- GARWON, M., DARMADI, L. H., URZYNICOK, F., BÄRWOLFF, G. & KING, R. 2003 Adaptive control of separated flow. In *Proc. European Control Conf. ECC'03, ECC Paper* 543.
- GELB, A. 1986 *Applied Optimal Estimation*. The MIT Press.
- GERHARD, J., PASTOOR, M., KING, R., NOACK, B. R., DILLMANN, A., MORZYŃSKI, M. & TADMOR, G. 2003 Model-based control of vortex shedding using low-dimensional Galerkin models. *AIAA Paper* 2003-4262.
- GHONIEM, A. F. & GAGNON, Y. 1987 Vortex simulation of laminar recirculating flow. *J. Comput. Phys.* **68**, 346–377.
- GIESING, J. P. 1969 Vorticity and Kutta condition for unsteady multi-energy flows. *Trans. ASME: J. Appl. Mech.* **36**, 608–613.

- GROSCHKE, F. R. & MEIER, G. E. A. 2001 Research at the DLR Göttingen on bluff body aerodynamics, drag reduction by wake ventilation and active flow control. *J. Wind. Engng Ind. Aerodyn.* **89**, 1201–1218.
- HELMHOLTZ, H. 1858 Über Integrale der hydrodynamischen Gleichungen, welche den Wirbelbewegungen entsprechen. *Crelles J.* **55**, 25–55.
- HENNING, L. & KING, R. 2005a Multivariable closed-loop control of the reattachment length downstream of a backward-facing step. In *Proc. 16th IFAC World Congress. IFAC Paper* 02575.
- HENNING, L. & KING, R. 2005b Drag reduction by closed-loop control of a separated flow over a bluff body with a blunt trailing edge. In *Proc. 44th IEEE Conf. on Decision and Control and European Control Conference CDC-ECC'05*, pp. 494–499.
- HENNING, L. & KING, R. 2007 Robust multivariable closed-loop control of a turbulent backward-facing step flow. *J. Aircraft* **40**, 201–208.
- HENNING, L., PASTOOR, M., KING, R., NOACK, B. R. & TADMOR, G. 2007 Feedback control applied to bluff body wake. In *Active Flow Control* (ed. R. King). Notes on Numerical Fluid Mechanics and Multidisciplinary Design, vol. 95. Springer.
- HUCHO, W.-H. 2002 *Aerodynamik der stumpfen Körper. Physikalische Grundlagen und Anwendungen in der Praxis*. Vieweg.
- HUERRE, P. & MONKEWITZ, P. A. 1990 Local and global instabilities in spatially developing flows. *Annu. Rev. Fluid Mech.* **22**, 473–537.
- VON KÁRMÁN, T. 1911 Über den Mechanismus des Widerstandes, den ein bewegter Körper in einer Flüssigkeit erfährt. *Nachrichten der Kaiserlichen Gesellschaft der Wissenschaften zu Göttingen*, pp. 324–338.
- KIM, J., HAHN, S., LEE, D., CHOI, J., JEON, W.-P. & CHOI, H. 2004 Active control of turbulent flow over a model vehicle for drag reduction. *J. Turb.* **5**, 1–25.
- KING, R., BECKER, R., GARWON, M. & HENNING, L. 2004 Robust and adaptive closed-loop control of separated shear flows. *AIAA Paper* 2004-2519.
- KING, R., SEIBOLD, M., LEHMANN, O., NOACK, B. R., MORZYŃSKI, M. & TADMOR, G. 2005 Nonlinear flow control based on a low dimensional model of fluid flow. In *Control and Observer Design for Nonlinear Finite and Infinite Dimensional Systems* (ed. T. Meurer *et al.*). Lecture Notes in Control and Information Sciences, vol. 322, pp. 369–386. Springer.
- KRASNY, R. 1986 Desingularization of periodic vortex sheet roll-up. *J. Comput. Phys.* **65**, 292–313.
- KRSTIĆ, M. & WANG, H.-H. 2000 Stability of extremum seeking feedback for general nonlinear dynamic systems. *Automatica* **36**, 595–601.
- LEDER, A. 1992 *Abgelöste Strömungen – Physikalische Grundlagen*. Vieweg.
- LEONARD, A. 1985 Computing three-dimensional incompressible flows with vortex elements. *Annu. Rev. Fluid Mech.* **17**, 523–559.
- LITTLE, J., DEBIASI, M., CARABALLO, E., & SAMIMY, M. 2007 Effects of open-loop and closed-loop control on subsonic cavity flows. *Phys. Fluids* **19**, 065104.
- LUGT, H. J. 1996 *Introduction to Vortex Theory*. Vortex Flow Press.
- LUMLEY, J. L. & BLOSSEY, P. N. 1998 Control of turbulence. *Annu. Rev. Fluid Mech.* **30**, 311–327.
- MEIBURG, E. 1995 Three-dimensional vortex dynamics simulation. In *Fluid Vortices* (ed. S. Green), pp. 651–685. Kluwer.
- MERCKER, E. 1980 Eine Blockierungskorrektur für aerodynamische Messungen in offenen und geschlossenen Unterschallwindkanälen. PhD Thesis, Technische Universität Berlin.
- MILNE-THOMSON, L. M. 1968 *Theoretical Hydrodynamics*. Macmillan.
- NOACK, B. R., AFANASIEV, K., MORZYŃSKI, M., TADMOR, G. & THIELE, F. 2003 A hierarchy of low-dimensional models for the transient and post-transient cylinder wake. *J. Fluid Mech.* **497**, 335–363.
- NOACK, B. R., PAPAS, P. & MONKEWITZ, P. A. 2005 The need for a pressure-term representation in empirical Galerkin models of incompressible shear flows. *J. Fluid Mech.* **523**, 339–365.
- NOACK, B. R., TADMOR, G. & MORZYŃSKI, M. 2004 Low-dimensional models for feedback flow control. Part I: Empirical Galerkin models (Invited). *AIAA Paper* 2004-2408.
- PARK, H., LEE, D., JEON, W.-P., HAHN, S., KIM, J., KIM, J., CHOI, J. & CHOI, H. 2006 Drag reduction in flow over a two-dimensional bluff body with a blunt trailing edge using a new passive device. *J. Fluid Mech.* **563**, 389–414.

- PASTOOR, M., KING, R., NOACK, B. R., DILLMANN, A. & TADMOR, G. 2003 Model-based coherent-structure control of turbulent shear flows using low-dimensional vortex models. *AIAA Paper* 2003-4261.
- PROTAS, B. 2004 Linear feedback stabilization of laminar vortex shedding based on a point vortex model. *Phys. Fluids* **16**, 4473–4488.
- PROTAS, B. 2006 Higher-order Föppl models of steady wake flows. *Phys. Fluids* **18**, 117109.
- PROTAS, B. & WESFREID, J.-E. 2002 Drag force in the open-loop control of the cylinder wake in the laminar regime. *Phys. Fluids* **14**, 810–826.
- ROSENHEAD, L. 1931 The formation of vortices from a surface of discontinuity. *Proc. R. Soc. Lond.* **134**, 170–192.
- ROUSSOPOULOS, K. 1993 Feedback control of vortex shedding at low Reynolds numbers. *J. Fluid Mech.* **248**, 267–296.
- ROWLEY, C. W., WILLIAMS, D. R., COLONIUS, T., MURRAY, R. M., MACMARTIN, D. G. & FABRIS, D. 2002 Model-based control of cavity oscillations. Part II: System identification and analysis. *AIAA Paper* 2002-0972.
- SEIDEL, J., SIEGEL, S., COHEN, K., BECKER, V. & MCLAUGHLIN, T. 2007 Simulations of three dimensional feedback control of a circular cylinder wake. *AIAA Paper* 2006-1404.
- SIEGEL, S., ARADAG, S., SEIDEL, J., COHEN, K. & MCLAUGHLIN, T. 2007 Low dimensional POD based estimation of a 3D turbulent separated flow. *AIAA Paper* 2007-0112.
- SIEGEL, S., COHEN, K. & MCLAUGHLIN, T. 2003 Feedback control of a circular cylinder wake in experiment and simulation. *AIAA Paper* 2003-3571.
- SIEGEL, S., COHEN, K., SEIDEL, J., LUCHTENBURG, M. & MCLAUGHLIN, T. 2008 Low dimensional modelling of a transient cylinder wake using double proper-orthogonal decomposition. *J. Fluid Mech.* (in press).
- SOTERIOU, M. 2003 Vortex element method – expansion about incompressible flow computation of noise generation by subsonic shear flows – the impact of external forcing. *J. Turb.* **4**, 1–9.
- TADMOR, G. 2004 Observers and feedback control for a rotating vortex pair. *IEEE Trans. Control Systems Technol.* **12**, 36–51.
- TADMOR, G., NOACK, B. R., MORZYŃSKI, M. & SIEGEL, S. 2004 Low-dimensional models for feedback flow control. Part II: Observer and controller design (Invited). *AIAA Paper* 2004-2409.
- TANG, S. & AUBRY, N. 2000 Suppression of vortex shedding inspired by a low-dimensional model. *J. Fluids Struct.* **14**, 443–468.
- TANNER, M. 1972 A method of reducing the base drag of wings with blunt trailing edges. *Aeronaut. Q.* **23**, 15–23.
- THOMSON, W. 1869 On vortex motion. *Trans. R. Soc. Edin.* **25**, 217–260.
- TOMBAZIS, N. & BEARMAN, P. W. 1997 A study of three-dimensional aspects of vortex shedding from a bluff body with a mild geometric disturbance. *J. Fluid Mech.* **330**, 85–112.
- WU, C.-J., WANG, L. & WU, J.-Z. 2007 Suppression of the von Kármán vortex street behind a circular cylinder by a travelling wave generated by a flexible surface. *J. Fluid Mech.* **574**, 365–391.
- WU, C.-J., XIE, Y. & WU, J.-Z. 2003 Fluid roller bearing effect and flow control. *Acta Mechanica Sinica* **19** (5), 476–484.
- WYGNANSKI, I. 2004 The variables affecting the control of separation by periodic excitation. *AIAA Paper* 2004-2505.
- ZHANG, H.-Q., FEY, U., NOACK, B. R., KÖNIG, M. & ECKELMANN, H. 1995 On the transition of the cylinder wake. *Phys. Fluids* **7**, 779–794.